International Journal of Nanomedicine

Dovepress
open access to scientific and medical research

Open Access Full Text Article

ORIGINAL RESEARCH

Hollow Hydroxyapatite Microspheres Loaded with rhCXCL13 to Recruit BMSC for Osteogenesis and Synergetic Angiogenesis to Promote Bone Regeneration in Bone Defects

Jianhua Zeng[1,2,*], Shilang Xiong[3,*], Jingyu Zhou[4], Peng Wei[4], Kai Guo[1], Feng Wang[1], Min Ouyang[4], Zhisheng Long[5], Aihua Yao[6], Jingtang Li[7], Long Xiong[4], Desheng Wu[1]

[1]Department of Spine Surgery, Shanghai East Hospital, School of Medicine, Tongji University, Shanghai, 200092, China; [2]Department of Spine Surgery, People's Hospital of Ganxian District, Ganzhou, Jiangxi, 341100, China; [3]Department of Orthopedics, the First Affiliated Hospital of Nanchang University, Artificial Joints Engineering and Technology Research Center of Jiangxi Province, Nanchang, Jiangxi, 330006, China; [4]Department of Orthopedics, Second Affiliated Hospital of Nanchang University, Nanchang, Jiangxi, 330006, China; [5]Department of Spine Surgery, Jiangxi Provincial People's Hospital the First Affiliated Hospital of Nanchang Medical College, Nanchang, Jiangxi, 330006, China; [6]School of Materials Science and Engineering, Tongji University, Shanghai, 201804, China; [7]Department of Traumatology, Jiangxi provincial People's Hospital the First Affiliated Hospital of Nanchang Medical College, Nanchang, Jiangxi, 330006, China

*These authors contributed equally to this work

Correspondence: Desheng Wu; Long Xiong, Email 1300116@tongji.edu.cn; ncxionglong2@126.com

Introduction: Bone tissue engineering is a promising method to treat bone defects. However, the current methods of preparing composite materials that mimic the complex structure and biological activity of natural bone are challenging for recruitment of bone marrow mesenchymal stem cells (BMSCs), which affects the application of these materials in situ bone regeneration. Hollow hydroxyapatite microspheres (HHMs) possess a natural porous bone structure, good adsorption, and slow release of chemokines, but have low ability to recruit BMSCs and induce osteogenesis. In this study, The HHM/chitosan (CS) and recombinant human C-X-C motif chemokine ligand 13 (rhCXCL13)-HHM/CS biomimetic scaffolds that optimize bone regeneration and investigated their mechanism of BMSC recruitment and osteogenesis through cell and animal experiments and transcriptomic sequencing.

Methods: Evaluate the physical characteristics of the HHM/CS and rhCXCL13-HHM/CS biomimetic scaffolds through Scanning Electron Microscopy (SEM), X-Ray Diffraction (XRD), and the cumulative release curve of rhCXCL13. Transwell migration experiments and co-culture with BMSCs were conducted to study the recruitment ability and osteogenic differentiation of the scaffolds. Transcriptomic sequencing was performed to analyze the osteogenic differentiation mechanism. The osteogenesis and bone healing performance were evaluated using a rabbit radial defect model.

Results: SEM demonstrated that the rhCXCL13-HHM/CS scaffold comprised hydroxyapatite microspheres in a porous three-dimensional network. The rhCXCL13 showed excellent sustained release capability. The rhCXCL13-HHM/CS scaffold could recruit BMSCs and induce bone regeneration. Transcriptome sequencing and experimental results showed that the osteogenesis mechanism of rhCXCL13-HHM/CS was through the PI3K-AKT pathway. In vivo, the rhCXCL13-HHM/CS scaffold significantly promoted osteogenesis and angiogenesis at 12 weeks after surgery.

Conclusion: The rhCXCL13-HHM/CS scaffold demonstrates excellent potential for BMSC recruitment, osteogenesis, vascularized tissue-engineered bone reconstruction, and drug delivery, providing a theoretical basis for material osteogenesis mechanism study and promising clinical applications for treating large bone defects.

Keywords: bone regeneration, rhCXCL13-HHM/CS scaffold, recruit BMSCs, transcriptome sequencing, bone repair

Received: 16 February 2023
Accepted: 19 June 2023
Published: 29 June 2023

Introduction

Large refractory bones with poor blood circulation, large scope or weakened osteogenic capacity have been a great challenge for orthopaedic surgeons.[1] Multiple surgeries are required, resulting in poor efficacy and even amputation, which imposes a substantial economic and social burden on patients. Currently, autologous bone graft with vascular pedicle remains the gold standard for clinical bone repair. However, this operation has several disadvantages, limited quantities available, large surgical wounds, strict surgical requirements, and unsatisfying vascular ingrowth. Large bone allograft only plays a supporting role in the process due to inferior osteoinductive capability and lack of blood supply.[2,3] In bone tissue engineering, tissue engineering bone is the most promising new bone repair material. The classic tissue engineering bone contains seed cells, scaffold materials, and osteogenic related active factors. The seed cells should be stable in origin, easy to obtain, and have the ability to proliferate and differentiate.[4,5] At present, the seed cells used for bone tissue engineering are mainly bone marrow mesenchymal stem cells, which have strong proliferative capacity and great osteogenic differentiation potential, and are conducive to bone tissue repair. Allogeneic and autologous bone-derived marrow mesenchymal stem cells have complications such as rejection, infection and local injury when applied in clinical management, the reimplantation of cultured bone marrow mesenchymal stem cells will affect the cell activity and function. The recruitment of autologous endogenous stem cells can avoid the complications mentioned above, and the source of bone marrow mesenchymal stem cells in local bone tissue is rich.

Chemokines are small secreted proteins which can induce cellular chemotaxis, with a molecular weight of 8~12kDa and consisting of 80–120 amino acids, making them the largest cytokine family.[6] They induce the directional migration of target cells by binding to the G protein-coupled receptors on the cell membrane. Chemokine-mediated directional migration of stem cells plays a key role in the homing of MSCs.[7] For example, in the directional migration of MSCs,[8] CXCL13 is a crucial chemokine that mediates MSCs into injured bone tissue[7] and promotes MSCs to differentiate into endothelial cells. Therefore, CXCL13 is introduced into various biomaterials to improve biological effects. CXCL13 is only expressed in osteoblast precursor cells among various chemokines secreted by bone tissue. It specifically binds to the receptor CXCR5 (chemokine C-X-C subfamily receptor5) to mediate the targeted migration, proliferation and differentiation of target cells, which can improve angiogenesis and bone stimulation.[7,9,10] Luttichau[11] finds that CXCR5 exists on mesenchymal stem cells (MSCs) surface. The researcher also confirms that CXCL13 has good chemotactic activity in MSCs and promotes osteogenesis and angiogenesis differentiation. However, few people notice the chemotactic effect of CXCL13 loaded with hollow hydroxyapatite microspheres and the mechanism of osteogenesis and angiogenesis. Here, the recombinant human chemokine CXCL13 (rhCXCL13) is introduced. And hollow hydroxyapatite microspheres load recombinant human CXCL13 (rhCXCL13), which theoretically has stronger chemotaxis and osteogenic differentiation ability. It provides a theoretical basis for the chemotactic mechanism of MSCs' directional migration and the regulation mechanism of osteogenesis and angiogenesis.

Hydroxyapatite (HA) is the main inorganic compound in bones and teeth. It is widely used as the biomaterial for bone regeneration due to its excellent biocompatibility and osteoconductivity.[12] The hollow hydroxyapatite microsphere is made through the in-situ transformation of borate glass. It has a porous surface and hollow interior hydroxyapatite microsphere with a specific high surface area (>100m^2/g). This unique structure enhances drug loading and enables sustained, controlled release of loaded bioactive molecules. It is an ideal drug carrier with efficacy in bone tissue regeneration, drug loading and release.[13]

In previous studies, hollow hydroxyapatite (HA) microspheres were successfully synthesized through an in-situ reaction. These microspheres featured a size range of 97–154 μm and were characterized by their hollow interiors. A layered porous HA/CS (chitosan) scaffold was constructed for bone regeneration, which demonstrated superior osteogenic and angiogenic capabilities due to it have more complex heterogeneous morphology and structure compared to the unipolar HA/CS scaffold. A rhBMP2-HA/CS scaffold for bone regeneration[14] was further constructed. It performed a strong bone healing ability, and biological activity in the rabbits with radius bone defects[15] and significantly increased blood vessel quantity in new bone tissues, which indicates that the

morphology and structure of the scaffold have biological effects on osteogenesis and vascular differentiation.[16] However, maximizing rhBMP-2 function in bone repair is difficult owing to the lack of sufficient osteoblast precursors and stem cells in the local bone defect. Therefore, bone formation can be more conducive if bone marrow mesenchymal stem cells can be recruited in bone defect areas.

In this study, HHMs microspheres are first in situ transposition from borate glass and loaded with recombinant human CXCL13 (rhCXCL13-HHMs). Then the rhCXCL13-HHMs is added to the chitosan matrix to construct an rhCXCL13-HHM/CS biomimetic scaffold (rhCXCL13-HHM/CS) through the highly bionic mixed cross-linked natural bone structure. In vitro, the HHM/CS and rhCXCL13-HHM/CS scaffolds firstly recruit rat bone marrow mesenchymal stem cells, and then verify the osteogenic differentiation effect. Concurrently, the biological properties and osteogenesis of the scaffolds are studied with rat BMSCs co-culture. Later, the mechanism of osteogenesis is explored through transcriptome sequencing. Finally, the rabbit radial defect model is used to further evaluate bone regeneration and biomimetic scaffold angiogenesis in vivo. The complete research process is depicted in Scheme 1.

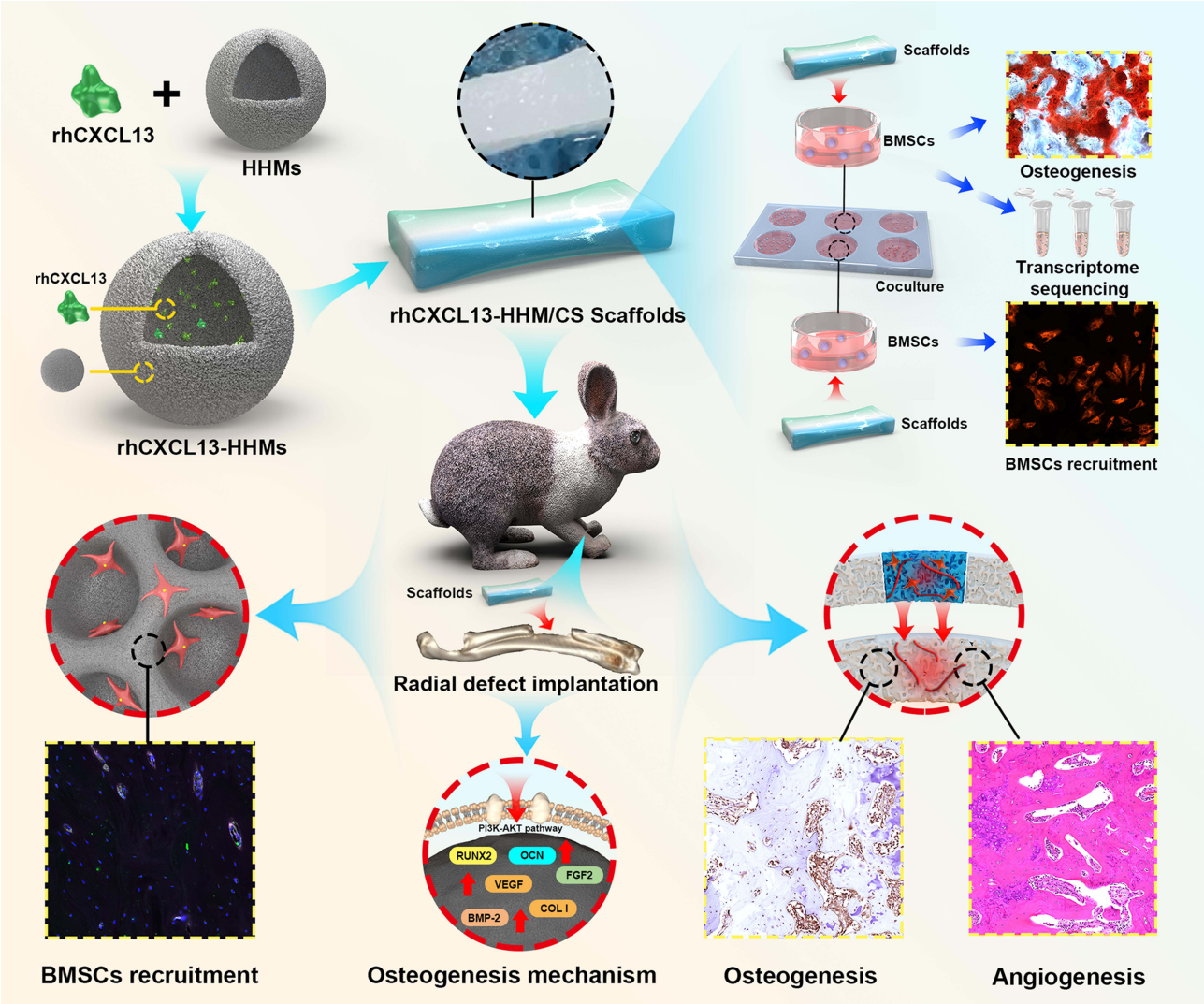

Scheme 1 Schematic diagram of radial defect treatment using rhCXCL13-HHM/CS scaffold: In vitro studies demonstrate that the rhCXCL13-HHM/CS scaffold promotes osteogenic differentiation of bone marrow mesenchymal stem cells, while in vivo experiments facilitate seamless adhesion and regeneration within bone defect areas. The scaffold recruits endogenous bone marrow mesenchymal stem cells, initiation of osteogenesis and angiogenesis, and realization of radial reconstruction. Twelve weeks post-implantation, the scaffold achieves extensive bone regeneration, with the bone coverage area in the rabbit radial defect model reaching 95%.

Materials and Methods

Materials

Li2CO3, CaCO3, H3BO3, β-Sodium glycerophosphate, and chitosan were obtained from Aladdin (Shanghai, China). K2HPO4 was procured from Tianjin Zhiyuan Chemical Reagent (Tianjin, China). Recombinant human CXCL13 (rhCXCL13) was provided by PeproTech (State of New Jersey, USA), while Bone Marrow Stromal Cells (BMSCs) were sourced from the Chinese Academy of Sciences (Shanghai, China). The Trizol, and HiScript® III RT SuperMix kit were acquired from Vazyme (Nanjing, China), whereas fetal bovine serum (FBS) was obtained from Gibco (New Zealand). Calcein-AM/PI kit was purchased from Maokang (Shanghai, China). Runx2, OCN, and ALPL primer were supplied by Sangon Biotech (Shanghai, China), and OriCellSD® rat osteogenic differentiation medium was procured from Saiye (Guangzhou, China). PI3K-AKT inhibitor BEZ235 was obtained from Selleck (Shanghai, China) and EDU was obtained from Beyotime (Shanghai, China). Transwell plates were sourced from Corning (New York, USA). Cell Counting Kit-8, Anti-Runx2 antibody, Anti-OCN antibody, Anti-BMP2 antibody, Anti-COL I antibody, anti-GAPDH antibody, and HRP Goat Anti-Rabbit IgG (H+L) were provided by ABclonal (Wuhan, China). The α-MEM, PBS was acquired from Servicebio (Wuhan, China).

Preparation of HHMs, rhCXCL13-HHMs

The Li-Ca-B glass (LCB glass) of 10LiO-10CaO-80B2O3 (wt%) was prepared by the high-temperature melting method. Take 1.194g Li2CO3 (Aladdin, Shanghai, China), 1.786g CaCO3 (Aladdin, Shanghai, China), 14.207g H3BO3 (Aladdin, Shanghai, China) powder respectively and mix them evenly. Melt in a platinum crucible at 1100 °C for 25min to obtain bubble-free liquid glass, and then quench the molten glass between two stainless steel plates to obtain transparent crystallization-free glass. After the glass is broken and sieved, take Φ (97–154) um glass particles. The LCB glass microspheres are obtained by repeatedly spheroidizing the particles with flame spraying. Take 0.5g of spheroidized LCB glass powder and soak it in 50mL of 0.25mol/L K2HPO4 (Tianjin Zhiyuan Chemical Reagent Co., Ltd., China) solution (PH=9.0) in 37 °C constant temperature for two days. The sample was then removed from the soaking solution and rinsed three times with deionized water, dried thoroughly in an oven at 90 °C for 24h and calcinated at 600 °C for two hours, followed by furnace cooling to room temperature to obtain hollow hydroxyapatite microspheres (HHMs), sterilize them in absolute ethanol and dried under vacuum at 100 °C, 90Pa (Kangheng, Guangzhou, China) for standby. According to previous research, rhCXCL13 (PeproTech.USA) was loaded by vacuum drying method: rhCXCL13 was adsorbed to HHMs under pressure infiltration. The specific steps are as follows: [1] Prepare PBS buffer solution with a pH value of 7.2–7.4 according to the conventional method, and respectively dissolve 50ug rhCXCL13 in 500uL PBS (final concentration is 0.1 mg/mL), stored at 0–4 °C; [2] 500uL rhCXCL13 and 200mg HHMs were respectively placed in 2mL centrifuge tubes, and vacuum centrifuged at 0–4 °C to make rhCXCL13 diffuse into HHMs.

Preparation of HHM/CS, rhCXCL13-HHM/CS Scaffold

0.2 g CS is dissolved in 9 mL (0.1 M) hydrochloric acid solution, magnetic stirring for 12 h. Dissolute and filtrate it to obtain a transparent CS solution in aseptic conditions. The pH was adjusted with 1 M NaHCO3 to a pH>7.0. 560 mg β- Sodium glycerophosphate (Aladdin, Shanghai, China) is dissolved in 1 mL deionized water and dissolved by ultrasonic wave for 10s. GP solution is slowly dropped into CS solution with gentle stirring to obtain CS temperature-sensitive hydrogel. Afterwards, 20 mg HHMs and rhCXCL13 HHMs are separately added. Stir the mixture to avoid precipitation. Obtain a stable composite hydrogel at room temperature. Hydrogel is injected into the cylindrical model (L=12mm, Φ= 10mm) and stored in 38 °C constant temperature humectant for 24 hours to make it completely gel to obtain HHM/CS, rhCXCL13-HHM/CS biomimetic scaffolds.

Characterization of HHM/CS, rhCXCL13-HHM/CS Scaffold

The phase composition of rhCXCL13-HHM/CS and HHM/CS scaffolds was analyzed by X-ray diffraction (XRD, Zeiss Sigma 300, Germany). Scanning electron microscopy (SEM, ZEISS Gemini 300, OXFORD Xplore) was used to observe the microstructure and cross-sectional morphology of the scaffold. RhCXCL13 drug release test: rhCXCL13-HHM/CS scaffold was soaked in 2mL PBS solution, and 10ul PBS solution was taken every interval to determine the drug release concentration by ELISA.

BMSC Osteogenesis in vitro

BMSCs Co-Cultures Respectively with HHM/CS and rhCXCL13-HHM/CS Scaffold

5x10 ^ 4 BMSCs (the Institute of Biochemistry and Cell Biology, Chinese Academy of Sciences, Shanghai, China) were seeded respectively per well using a 12-well plate. Add 1 mL of α-MEM (Servicebio, Wuhan, China) medium containing 10% FBS(Gibco) and 1% penicillin/streptomycin to each well, co-cultured with HHM/CS and rhCXCL13-HHM/CS, respectively. No material was added to the Blank group. BMSCs were used in passages 4 to 6 for all experiments. Cell media was changed every other day.

Live/Dead Cell Stain

To evaluate scaffolds biocompatibility, the BMSCs with scaffolds are co-cultured in a 12-well plate (Corning, NY, USA) for three days. BMSCs were stained with Calcein-AM/PI kit (Maokang Biotechnology, Shanghai, China) for living/dead cells to evaluate the survival rate of BMSCs. Specifically, the working solution contains 2 μM Calcein acetoxymethyl ester (AM) and 4.5 μM propidium iodide (PI). Add 200 ul of the staining working solution to the 12-well plate, then incubate it at 37 °C for 15 minutes before thoroughly cleaning it with PBS. Cells were calculated under a fluorescence microscope to determine the quantity and proportion of live and dead cells, followed by statistical analysis.

Cell Proliferation

Cell viability in proliferation and cytotoxicity assays was measured using the Cell Counting Kit-8 (ABclonal, China) for biocompatibility evaluation of the materials. In a 96-wells plate, 5 × 10 ^ 3 BMSCs were co-cultured with HHM/CS and rhCXCL13-HHM/CS. Following the CCK8 kit manufacturer's protocol, the CCK-8 solution was added daily from day 1 to day 6, after which all cells were co-cultured for 2 hours in a humidified incubator with 5% CO2 at 37 °C; subsequently, the light absorption value at 450 nm was measured using a microplate reader to evaluate the living cell quantity via optical density (OD) value, with cell viability expressed as a percentage.

To assess the proliferation of BMSCs, BMSCs were incubated with EDU (Beyotime Biotechnology, Shanghai, China) for six hours before being fixed, permeabilized, and stained for EDU and Hoechst. The cells were photographed a using fluorescence microscope. The proliferation was quantified by counting nuclei staining positive for EDU and normalizing the number to total nuclei.

BMSCs Recruitment in vitro

It will be precious if rhCXCL13-HHM/CS can actively recruit BMSCs. A transwell migration experiment was conducted to study the migration induction of bone marrow mesenchymal stem cells in the scaffolds. Transwell migration assays were performed using 24-well 8-μm pore Transwell plates (Corning, NY, USA). First, 2×10 ^ 4 BMSCs were plated in the upper chamber of αMEM medium, containing 10% FBS and 1% penicillin/streptomycin, put HHM/CS and rhCXCL13-HHM/CS scaffolds in the lower chamber. After 24 hours of culture, the medium was removed, and the cells were fixed with 4% paraformaldehyde and stained with 1% crystal violet. The quantity and proportion of the migrated cells were counted by taking pictures under the fluorescent microscope to evaluate the ability of the scaffold to recruit cells. Three holes were added to each group.

Osteogenesis Gene Expression Under Real-Time Quantitative PCR (RT-qPCR) Analysis

The expression levels of osteogenic differentiation-related genes of BMSCs co-cultured with HHM/CS and rhCXCL13 HHM/CS were detected by quantitative RT-PCR (qRT-PCR) to assess osteogenic potential. After 3-day culture of BMSCs, total RNA was extracted with Trizol (Vazyme Biotech Co., Ltd., Nanjing, China). 500 μg of RNA was reverse transcribed to complementary DNA (cDNA) using the HiScript® III RT SuperMix kit (Vazyme Biotech Co., Ltd., Nanjing, China). Transcripts of Runx2, OCN, and ALPL were amplified with Taq pro-Universal SYBR qPCR Master Mix on the 7500 software Real-Time PCR System (Applied Biosystems). Data were analyzed by the ΔΔCT method using GAPDH as the housekeeping gene.

Differentiation of BMSC

For co-culture experiments, 1x10^5 BMSCs were seeded separately in 6-well plates with HHM/CS and rhCXCL13 HHM/CS and cultured until the cells were ~80% confluent. 2mL of the OriCellSD® rat osteogenic differentiation medium (Saiye Biotechnology Co., Ltd., Guangzhou, China) was added to each well to induce osteogenic differentiation. The medium consists of 10 mM β-glycerophosphate, 50 μg/mL ascorbic acid and 0.1 μM dexamethasone. The cells were differentiated for 21 days with medium change every two days. After three weeks, cultures were washed and fixed with 4% paraformaldehyde for 10 min and stained using 2% Alizarin Red for the mineralized matrix for 15 min. The staining images were taken under a Leica microscope. The area of mineralized nodules per cultured well was quantified with image analysis, which uses ImageJ to evaluate the osteogenic differentiation ability of the two scaffolds. Similarly, based on transcriptomic sequencing results were used to verify whether the rhCXCL13-HHM/CS scaffold promotes BMSC osteogenesis through the PI3K/AKT pathway using the PI3K-AKT inhibitor BEZ235. Specifically, bone marrow mesenchymal stem cells were co-cultured with the rhCXCL13-HHM /CS scaffold according to the above protocol, with the addition of BEZ235 to achieve a medium concentration of 1uM. After 21 days of osteogenic differentiation culture, osteogenic differentiation changes were assessed using Alizarin Red staining, microscopic imaging, and statistical analysis of the mineralized nodule area."

Western Blotting Osteogenic Protein Analysis

The expression levels of RUNX2 (ABclonal, China) and OCN (ABclonal, China) Osteogenesis–related genes of BMSCs co-cultured with HHM/CS and rhCXCL13 HHM/CS were analyzed by Western blotting. 5×10 ^ 4 BMSCs were seeded using a 6-well plate. Add 2 mL of α-MEM medium containing 10% FBS and 1% penicillin/streptomycin to each well. The cells are co-cultured with HHM/CS and rhCXCL13-HHM/CS, respectively. In the blank group, no material was added for co-culture. Using the transcriptome sequencing results to validate whether the rhCXCL13-HHM/CS scaffold osteogenesis is conducted via the PI3K/AKT pathway mechanism. PI3K-AKT inhibitor BEZ235 was used based on transcriptome sequencing and data analysis. The specific operations were as follows: Add BEZ235 to the BMSCs cocultured to make the concentration of the culture medium 1 uM and culture for three days. Then the total protein was extracted with RIPA lysis buffer. Proteins were extracted as follows: BMSCs were harvested from the 6-well plates and then washed in PBS (Servicebio, Wuhan, China) and lysed in RIPA buffer plus protease inhibitors cocktail. Lysates were centrifuged at 12,000 r for 10 min, and supernatants were transferred to a new EP tube. Protein quantification was performed using the BCA protein assay. 25 μg of each sample were loaded on a 12.5% Sodium dodecyl sulfate-polyacrylamide gel electrophoresis (SDS-PAGE). The membrane was blocked with 5% non-fat milk for one hour, followed by washing three times with TBST (Servicebio, Wuhan, China). After the washing, membranes were incubated with rabbit anti-RUNX2 (Abclonal; 1:1000), rabbit anti-OCN (Abclonal; 1:1000), and rabbit anti-GAPDH (Abclonal; 1:1000) antibodies at 4◦C overnight. Wash and incubate for two hours with anti-rabbit secondary antibodies. Membranes were then developed with enhanced chemiluminescence (ECL). Signal intensities were quantified with Image J and normalized to GAPDH.

Immunofluorometric Assay

Flame-sterilized 20 mm round glass coverslips were placed in sterile 12-well culture plates. BMSCs were plated separately on sterile coverslips (2x10^4 cells/well) and cultured for three days. The medium was removed. BMSCs were fixed with 4% paraformaldehyde for 20 min after washing with PBS three times. For immunofluorescence staining, BMSCs were permeabilized with 0.2% Triton X-100 (Beyotime Biotechnology, Shanghai, China) for 10 min. Sections were blocked for one hour with the blocking solution at room temperature and then transferred to RUNX2 (ABclonal, China), OCN (ABclonal, China), COLI (ABclonal, China), BMP-2 (ABclonal, China) of primary antibodies overnight at 4°temperature. After washing with PBS, cells were incubated for one hour with the secondary antibody at room temperature and counterstained with DAPI. Finally, the coverslips were sealed with an anti-fluorescence quenching agent. All procedures were performed at room temperature except where otherwise specified. ZEN2.3 software was used for image acquisition, and images were analyzed using ImageJ.

Transcriptome Sequencing and Data Analysis

RNA sequencing (RNA-seq) was performed to analyze gene expressions in cells on matrices of different scaffolds. It is significant to analyze the osteoblastic mechanism and signal transduction of different scaffold materials on BMSCs. BMSCs were plated in

12-well plates (2x10^4 cells/well) and co-cultured with HHM/CS and rhCXCL13 HHM/CS, respectively, for three days. After three days, cells were collected, centrifuged, lysed with TRIzol reagent, and snap-frozen. RNA-seq samples were sequenced using Illumina NovaSeq 6000 (American Illumina). The gene expression values (RPKM) were log10 transformed. Functional annotation enrichment analysis with KEGG pathway and Gene Ontology (GO) terms on differentially expressed genes was done using cluster Profiler (3.8.1). For protein-protein interaction analysis, information was used on known protein-protein interactions available in the STRING database to construct a functional protein association network.

Animal Experiment

Animal Surgery

The in vivo experiments used 36 New Zealand white adult male rabbits (weight:2.0–2.5Kg) aged 6 to 10 weeks. The model of the radius defect was established to observe the bone repair effect of the scaffold. Animals were randomized into three groups labeled as Blank, HHM/CS, rhCXCL13-HHM/CS group, and twelve animals were taken per group. The specific operation is as follows: All surgeries were performed on rats under general anaesthesia induced by intraperitoneal sodium pentobarbital (50 mg/kg). A 25 mm long skin incision was made in the skin along the forearm. Blunt dissection of muscle was used to expose the midshaft of the radius. 12 mm bone defects were made in the radius using a bone cutter. The periosteum was removed together. HHM/CS and rhCXCL13-HHM/CS scaffold materials were implanted, respectively, and no scaffold material was implanted in the Blank group. The incision was closed in two layers without securing the bone defect. Sterile gauze was used for dressing. For all animals, penicillin (20,000 IU/kg) and pyrazolone (0.1 mg/kg) were injected intramuscularly to prevent infection and analgesia for both on the day of surgery and daily after that for three days.

General Observation

Three New Zealand white rabbits were randomly selected from each group for euthanasia one, two and three months after surgery. The radius at the defect was taken out and photographed to observe the callus formation and material degradation of the bone defect.

X-Ray Analysis

In order to monitor the callus formation and bone healing, three animals in each group were randomly selected for lateral radiographs of the repaired limbs immediately after surgery and 4, 8 and 12 weeks after surgery. Lane-Sandhu histological scoring method for bone defect repair (Table 1):

Table 1 Scoring Standard of Lane-Sandhu Histological Scoring Method for Bone Defect Repair

	Evaluation Criteria	Score
Bone connectivity	No connections	0
	Fiber connection	1
	Connection of bone and osteoid	2
	Bone junction	3
	Complete regeneration of diaphysis	4
Cancellous bone	No osteocyte activity	0
	Early aggregation of new bone	1
	Active new bone aggregation	2
	Cancellous bone is being transformed	3
	Complete formation of cancellous bone	4
Cortical bone	No cortical bone growth	0
	Early manifestations of cortical bone growth	1
	Cortical bone is forming	2
	Most of the cortical bone is modified	3
	Complete bone regeneration	4

CT Analysis

In order to monitor the new bone formation and bone defect healing, three animals in each group were randomly selected for radial CT scanning immediately after surgery and 4, 8 and 12 weeks after surgery to analyze the callus growth in the bone defect area. After scanning, SkyScan NRecon software was used to reconstruct three-dimensional CT data. CTAn software (Skyscan Company) is used for image processing and statistical analysis by ImageJ for the new bone area and new bone cover area.

Histological Analysis

Animals sacrificed in each group were randomly selected 4, 8, and 12 weeks after surgery. The radial defect specimen was fixed with 4% paraformaldehyde solution for 24 h and decalcified using 10% ethylenediaminetetraacetic acid (EDTA, pH=7.4) for four weeks. Bones were dehydrated by a series of ethanol and embedded in paraffin and sectioned parallel to the long axis of radius five μM thickness. Hematoxylin-eosin (H&E) staining and Masson trichrome staining were performed to observe the bone tissue growth and material degradation of the implanted materials under the microscope. Images were taken with the Leica imaging system. The histomorphometry analysis of the histological images was performed using ImageJ software.

Immunohistochemical Analysis

Fixed specimens were decalcified with 10% EDTA (pH 7.4) for four weeks, dehydrated by a series of ethanol, embedded in paraffin and sectioned serially at 5 μm. The Paraffin section dewaxed to water and Antigen repair. Endogenous enzyme blocking sections were blocked for one hour with the blocking solution at room temperature and then transferred to RUNX2 and BMP-2 of primary antibodies overnight at 4°C. After washing with PBS, cells were incubated for one hour with Horseradish peroxidase (HRP) secondary antibody (anti-rabbit HRP) at room temperature and counterstained with DAPI. Finally, the coverslips were sealed with an anti-fluorescence quenching agent. All procedures were performed at room temperature except where otherwise specified. ZEN2.3 software was used for image acquisition, and images were analyzed using ImageJ.

Statistical Analysis

The data were analyzed by SPSS20.0 software. Three biological replicates were analyzed in each experiment. All data were expressed as mean ± standard deviations (SD). The statistical analysis was conducted through one-way analysis of variance (ANOVA), followed by LSD multiple comparison tests. All statistical analysis were based on a two-sided. The level of statistical difference between groups was defined as *P<0.05, **P<0.01, ***p< 0.001, NS indicates not statistical significance. Significant differences were defined at P<0.05.

Results

Physicochemical Properties of HHM/CS and rhCXCL13-HHM/CS Scaffold

Figure 1A and B are the Photographs of HHM/CS and rhCXCL13-HHM/CS scaffolds respectively. The structures of scaffolds are characterized by scanning electron microscopy (SEM) and X-ray diffraction (XRD). The SEM image shows that the prepared HHM/CS is a porous three-dimensional network structure. It has a clear and hollow mesoporous structure of particles (Figure 1C-F). SEM shows that the surface of the rhCXCL13-HHM/CS scaffold adsorbed more BMSCs, while the surface of the HHM/CS scaffold adsorbed fewer BMSCs (Figure 1G and H). The hollow structure of HHM with mesoporous is ideal for efficient drug loading. The unique surface and pore structure of hollow HA microspheres are crucial in HA microspheres' drug release performance. Researchers compare the XRD data of HHM/CS and rhCXCL13-HHM/CS and observe the rhCXCL13 load in the mesoporous and hollow HHM/CS. XRD analysis reveals distinct sharp peaks with high intensities (Figure 1I and J). The in vitro release kinetics shows that the rhCXCL13 of rhCXCL13-HHM/CS was released in vitro for 35 days. The first three days exhibited an initial burst release effect (Figure 1K) because rhCXCL13 adsorbed on the microspheres' surface was first dissolved after contacting PBS and then quickly released. After three days, rhCXCL13-HHM/CS showed excellent sustained release capability.

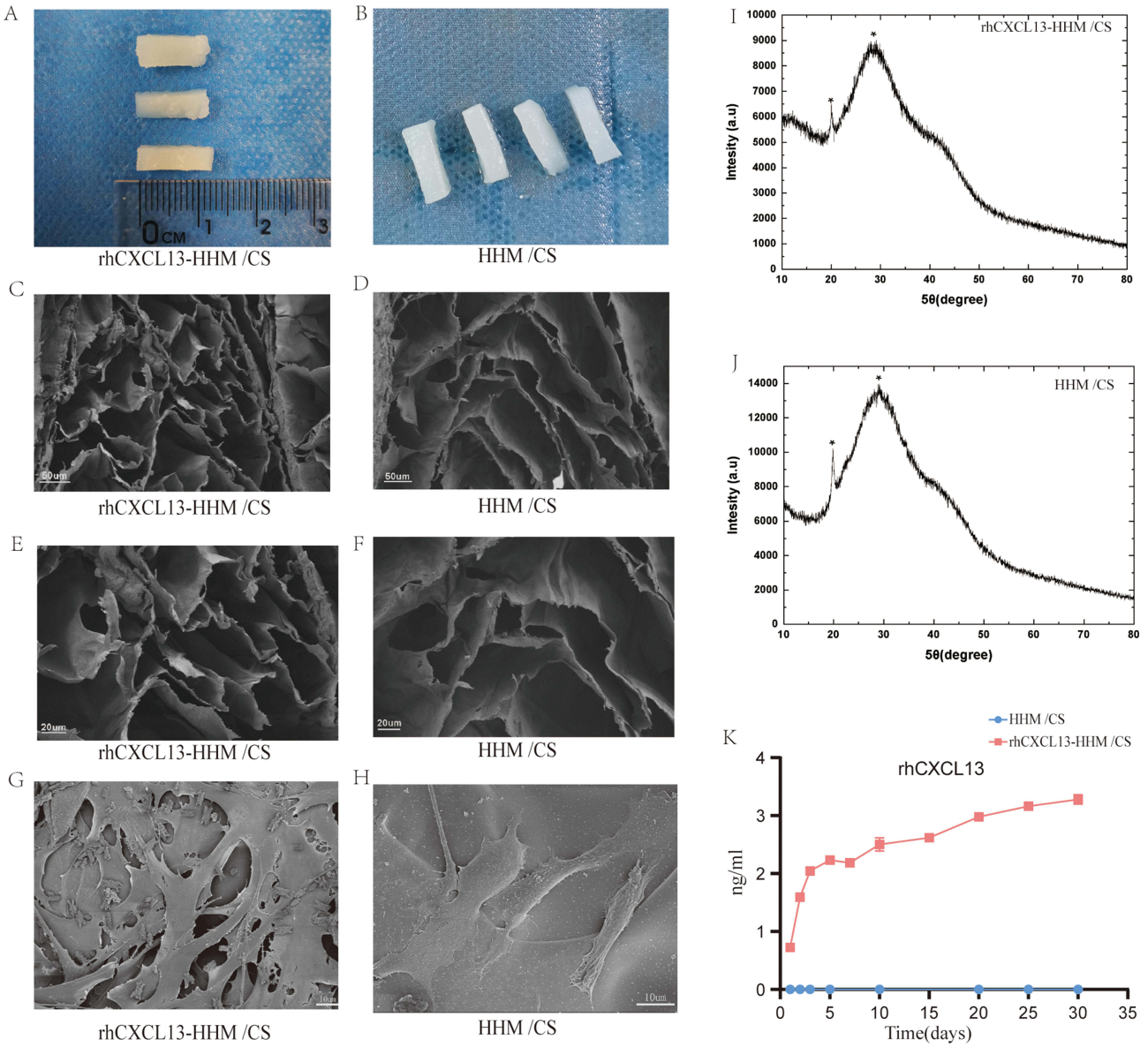

Figure 1 Physical characteristics and performance of HHM/CS and rhCXCL13-HHM/CS scaffolds: (**A** and **B**) Photographs of HHM/CS and rhCXCL13-HHM/CS scaffolds respectively. (**C-F**) SEM images revealing the scaffolds comprise hydroxyapatite microspheres in a porous three-dimensional network structure. ((**C** and **D**) scale bar=50um, (**E** and **F**) scale bar=20um). (**G** and **H**) SEM images of BMSCs adhesion on the scaffolds. The surface of the rhCXCL13-HHM/CS scaffold shows more adsorbed BMSCs, while fewer BMSCs are observed on the surface of the HHM/CS scaffold. (**I** and **J**) XRD of HHM/CS and rhCXCL13-HHM/CS scaffolds. (**K**) RhCXCL13 cumulative release curve in PBS solution over 35 days in vitro (n = 3).

In vitro Experiment of BMSCs

Cell Live/Dead Stain and Proliferation Experiment

Biocompatibility is the basis of implantable materials, and implantable biomaterials should have perfect biocompatibility and non-toxicity.[17] Therefore, researchers evaluate the in vitro biocompatibility and cell proliferation of rhCXCL13HHM/CS and HHM/CS. CCK-8 cell viability experiment demonstrated that all the materials can promote the proliferation of BMSCs in varying degrees after six days of co-culture. No difference is found among groups observed for cell proliferation on day 1, day 2, day 5 and day 6 (Figure 2A). On day 3 and day 4, the HHM/CS and rhCXCL13-HHM/CS group are significantly better than the blank group. CCK8 experiment proves that the material cam significantly promote BMSCs' proliferation on the third and fourth days because adding rhCXCL13 increases the proliferation and diffusion of cells. The live/dead staining is shown in Figure 2B. A few dead cells are detected on

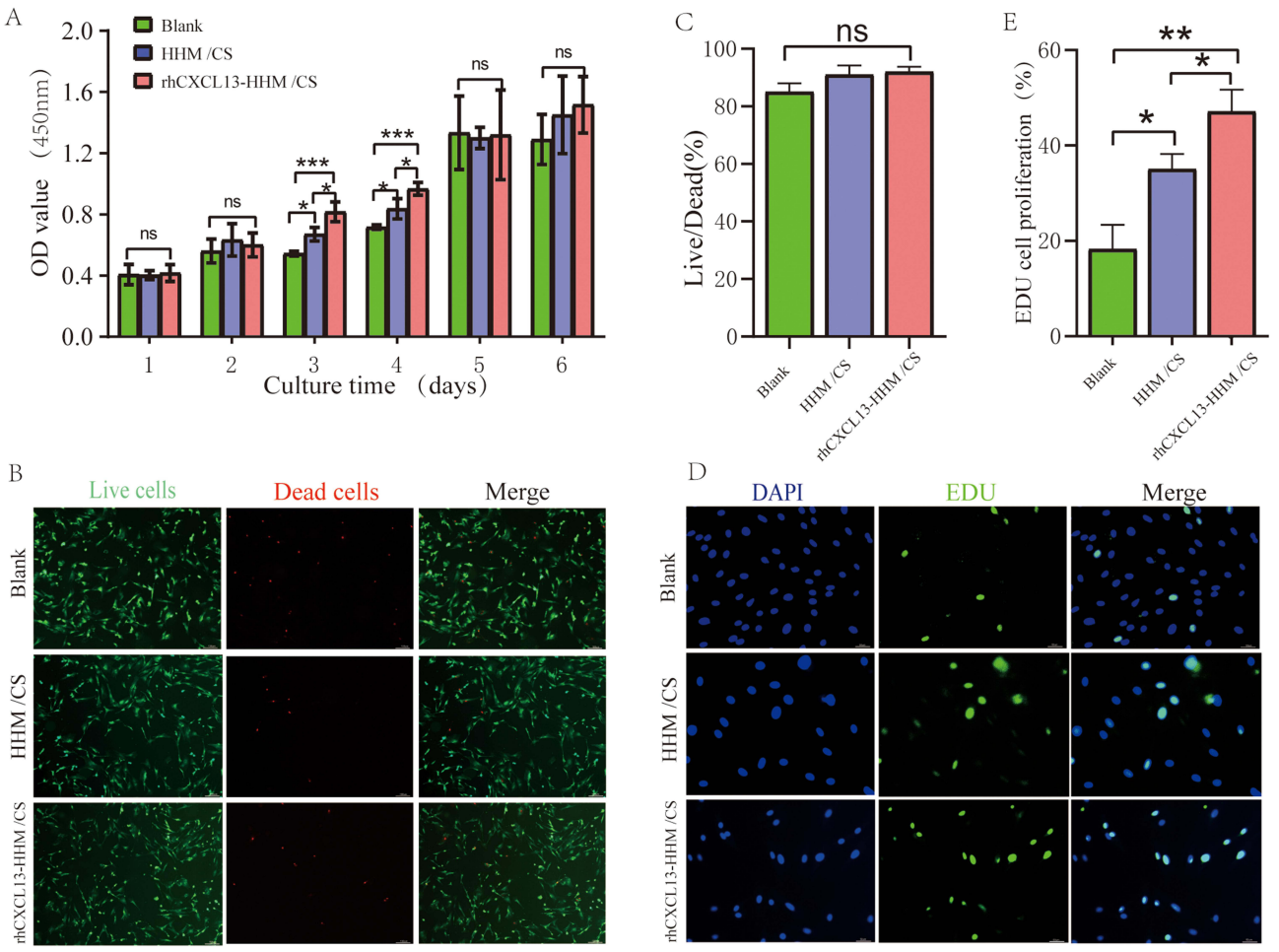

Figure 2 Biocompatibility and cell proliferation analysis of BMSCs co-cultured with different scaffolds. (**A**) CCK-8 cell viability assay of BMSCs co-cultured with various treatment groups for 1 day to 6 days. (**B**) Live/dead staining of BMSCs co-cultured with various treatment groups. (red = dead cells, green = live cells, scale bar = 100μm). (**C**) Quantitative analysis of live/dead cells staining indicates good biocompatibility and biosafety of the scaffolds (n = 3). (**D**) EdU staining of BMSCs co-cultured with various treatment groups (blue = DAPI, green = cell proliferation, scale bar = 100μm). (**E**) Quantitative analysis of EDU staining in BMSCs co-cultured with various treatment groups. ANOVA and LSD multiple comparison tests were used for statistical data analysis, with results expressed as mean ± SD (*p < 0.05, **p < 0.01, ***p < 0.001, n=3). **Abbreviation**: ns, Not statistical significance.

the surface of each sample of BMSCs. The ratio of live cells to dead cells is calculated. No statistical difference occurs in the live/dead ratio between groups (Figure 2C), indicating that the material has no toxic effect on cells. The live/dead staining results show that the HHM/CS and rhCXCL13-HHM/CS scaffold has excellent biocompatibility and non-toxicity. Meanwhile, EDU labeling (Figure 2D) is performed on the co-cultured BMSCs, and the EDU cell number is imaged and quantified. The cell proliferation of rhCXCL13-HHM/CS is significantly higher than the other two groups (Figure 2E). The EDU proliferation experiment shows that rhCXCL13-HHM/CS and HHM/CS scaffold are able to promote the proliferation of BMSCs. Meanwhile, there are found significant difference between the groups.

Cell Recruitment Assay

The transwell migration and crystal violet assays evaluate cell recruitment ability. Take pictures under a fluorescent microscope and quantitatively analyze the number and proportion of cells migrated. The Crystal violet staining results of BMSCs reveal that the quantity and proportion migrated to the rhCXCL13-HHM/CS group are higher than the other groups (Blank=8.00±2.65%, HHM/CS=13.67±3.21%, rhCXCL13-HHM/CS =21.67±3.05%) (Figure 3A and B). These phenomena indicate that rhCXCL13-HHM/CS has better chemotaxis and can recruit more BMSCs.

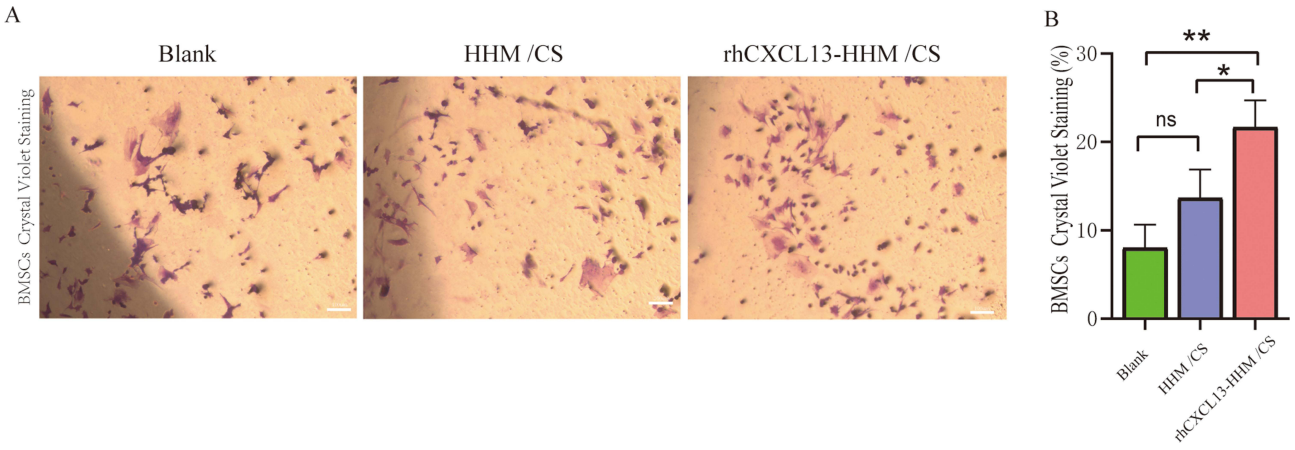

Figure 3 Scaffolds recruit BMSCs through transwell migration experiments. (**A**) Microscopic view of crystal violet-stained BMSCs migrating towards scaffolds. (**B**) Quantitative analysis of crystal violet-stained BMSCs migrating towards scaffolds. The data are statistically analyzed by ANOVA and LSD multiple comparison tests, with results expressed as mean ± SD (*p < 0.05, **p < 0.01, n=3).
Abbreviations: ns, Not statistical significance.

RT-qPCR, Western Blotting and Osteogenic Differentiation Analysis

The expression levels of osteogenesis-related genes, including Runx2, ALPL, and OCN, are validated by real-time quantitative polymerase chain reaction (RT-qPCR). Runx2, ALPL, and OCN express more in rhCXCL13-HHM/CS scaffold than that in HHM/CS and blank group (Figure 4A). The result indicates that the rhCXCL13-HHM/CS scaffold has better osteogenesis capacity than HHM/CS and the blank group.

Western Blotting analyzes Runx2 and OCN relative gene expression in each group and reveals that the expression is the highest in rhCXCL13-HHM/CS, followed by HHM/CS. The blank group is the lowest (Figure 4B). In vitro osteogenic differentiation experiment, all groups achieved good results regarding the osteogenic differentiation of BMSC (Figure 4C). Alizarin red quantitative analysis demonstrates that the rhCXCL13-HHM/CS scaffold group has the most mineralized nodules and the most uniform distribution, followed by HHM/CS. The blank group's mineralized nodules are in scattered distribution (Blank=41.00±3.61%, HHM/CS=53.33±2.52% and rhCXCL13-HHM/CS =67.67±2.52%, respectively) (Figure 4D). Mineralization degree may be related to the morphology of porous HHM/CS. Besides, rhCXCL13 can effectively promote the formation of mineralized nodules.

Immunofluorometric Assay

The osteogenic potential of scaffold-mediated cells in vitro was further examined through immunofluorescence (IF) staining (Figure 5). The immunofluorescence staining of BMSCs revealed the presence of fluorescence signals for Runx2, OCN, BMP2, and ColI in the Blank, HHM/CS, and rhCXCL13 HHM/CS groups (Figure 5A and B). Semi-quantitative analysis proves that stronger immunostaining of Runx2, OCN, BMP2, and Col1 occurs in the rhCXCL13 HHM/CS group, which reflects stronger osteogenic differentiation capacity (Figure 5a1, a2, b1 and b2). Thus, the immunofluorescence findings suggest that the osteogenic potential of the rhCXCL13-HHM/CS scaffold surpasses that of the other groups. Bone healing is a dynamic process guided by progenitor cells, necessitating synchronized osteogenesis and angiogenesis at the repair sites.[18] Consequently, the success of bone regeneration is also contingent on angiogenesis, plays a crucial role in bone tissue engineering.[19]

Transcriptomic Analysis of Osteogenic Differentiation Mechanism

To further analyze the osteogenic differentiation mechanism of rhCXCL13-HHM/CS, transcriptome sequencing is conducted. Transcriptomes of BMSCs co-culture with Blank, HHM/CS, and rhCXCL13 HHM/CS are sequenced. Pearson correlation analysis and principal component analysis assess the stability of the samples. Conduct intra-group and inter-group calculations on the correlation coefficient (R^2 value) of samples based on the gene of each

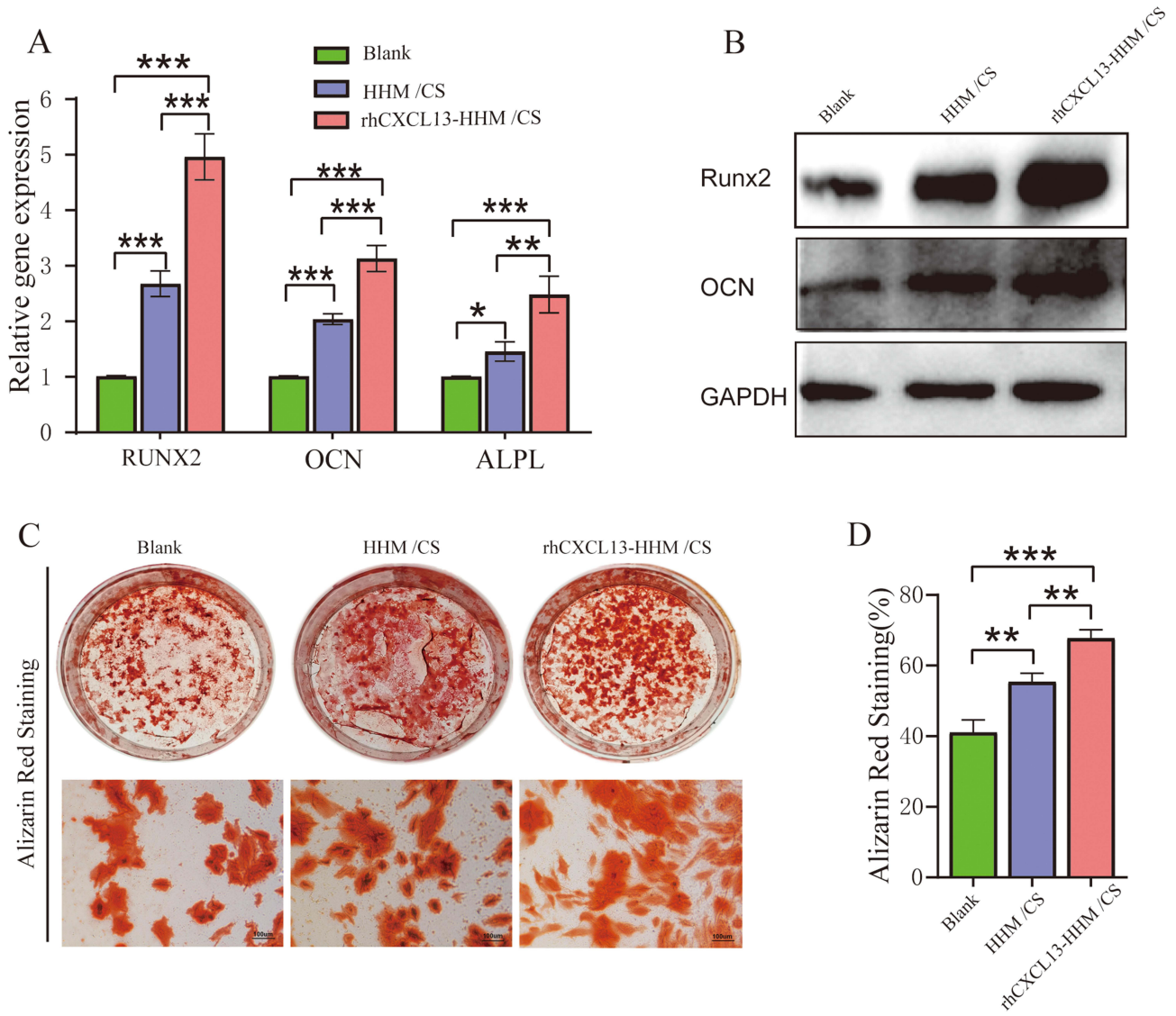

Figure 4 Analysis of osteogenic differentiation in BMSCs co-cultured with scaffolds. (**A**) Quantitative RT-qPCR analysis of osteogenic gene expression (Runx2, ALPL, OCN) in BMSCs co-cultured with each group. GAPDH was used as housekeeping genes. The results were expressed as mean ± SD. (**B**) Relative protein expression of RUNX2 and OCN in BMSCs co-cultured with various treatment groups. (**C**) Representative images of Alizarin red-stained BMSCs co-cultured with various scaffolds for 21 days in 6-well plates (scale bar = 100μm). (**D**) Quantitative analysis of Alizarin Red Staining in BMSCs co-cultured with various treatment groups. Statistical analysis was performed using ANOVA and LSD tests, with results expressed as mean ± SD (*p < 0.05, **p < 0.01, ***p < 0.001, n=3).

sample, and draw a correlation graph. The graph intuitively depicts the sample differences between groups and the duplication of samples within groups. Samples' correlation coefficients in each group are within the acceptable range (R^2>0.90, N=3) (Figure 6A), indicating excellent biological repeatability. The gene expression profile of all the samples under principal component analysis (PCA) shows that the transcriptome data could be used for further analysis (Figure 6B). The Venn diagram showed that the three groups shared 11,855 genes, with significant differential gene expression observed between them: 114 genes are differentially expressed between the Blank and HHM/CS groups, 202 genes between Blank and rhCXCL13-HHM/CS, and 126 genes between HHM/CS and rhCXCL13-HHM/CS (Figure 6C). Violin and Box map of differentially expressed genes as determined by transcriptome analysis (Figure 6D and E). The volcanic map shows that compared with the HHM/CS group, rhCXCL13-HHM/CS has 430 genes up-regulated and 193 genes down-regulated. Compared with the Blank group, rhCXCL13-HHM/CS has 60 genes up-regulated and 48 genes down-regulated. Between the Blank group and

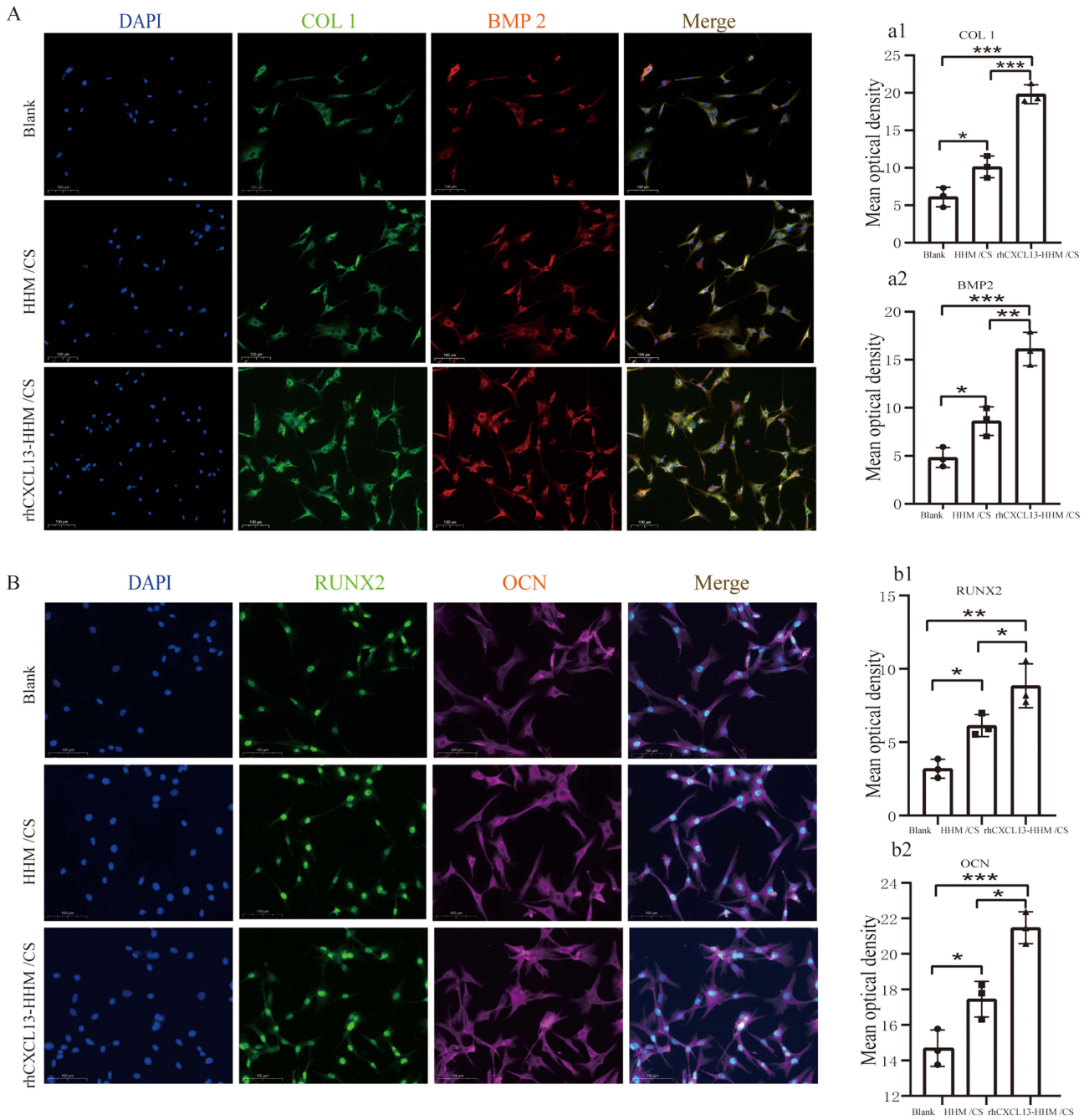

Figure 5 Immunofluorescence Staining Analysis of Osteogenic Differentiation in BMSCs Co-Cultured with Scaffolds. (**A**) Immunofluorescence staining of BMSCs (COLI, BMP-2, RUNX2, and OCN) when co-cultured with scaffolds ((**A** and **B**). (**B**) Quantitative analysis of immunofluorescence staining for COLI, BMP-2, RUNX2, and OCN performed by Image J. (**a1, a2, b1** and **b2**). Statistical analysis was performed using ANOVA and LSD tests, with results expressed as mean ± SD (*p<0.05, **p<0.01, ***p<0.001, n=3).

HHM/CS, HHM/CS has 185 genes up-regulated and 458 genes down-regulated (Figure 6F-H). Although HHM/CS and rhCXCL13-HHM/CS groups can promote bone healing, their mechanisms may vary.

The rhCXCL13-HHM/CS and HHM/CS scaffolds promote osteogenesis in vitro. However, the mechanisms underlying this process require further elucidation. Based on the functional enrichment analysis of differentially expressed genes (Figure 7A1-A3), these mechanisms can be specifically categorized into four types: cellular activity, osteogenesis, angiogenesis, and BMSC recruitment. Data were collected from rhCXCL13-HHM/CS and HHM/CS, HHM/CS and Blank for analysis in the Gene Ontology (GO) database. (Figure 7B1-B3). In HHM/CS

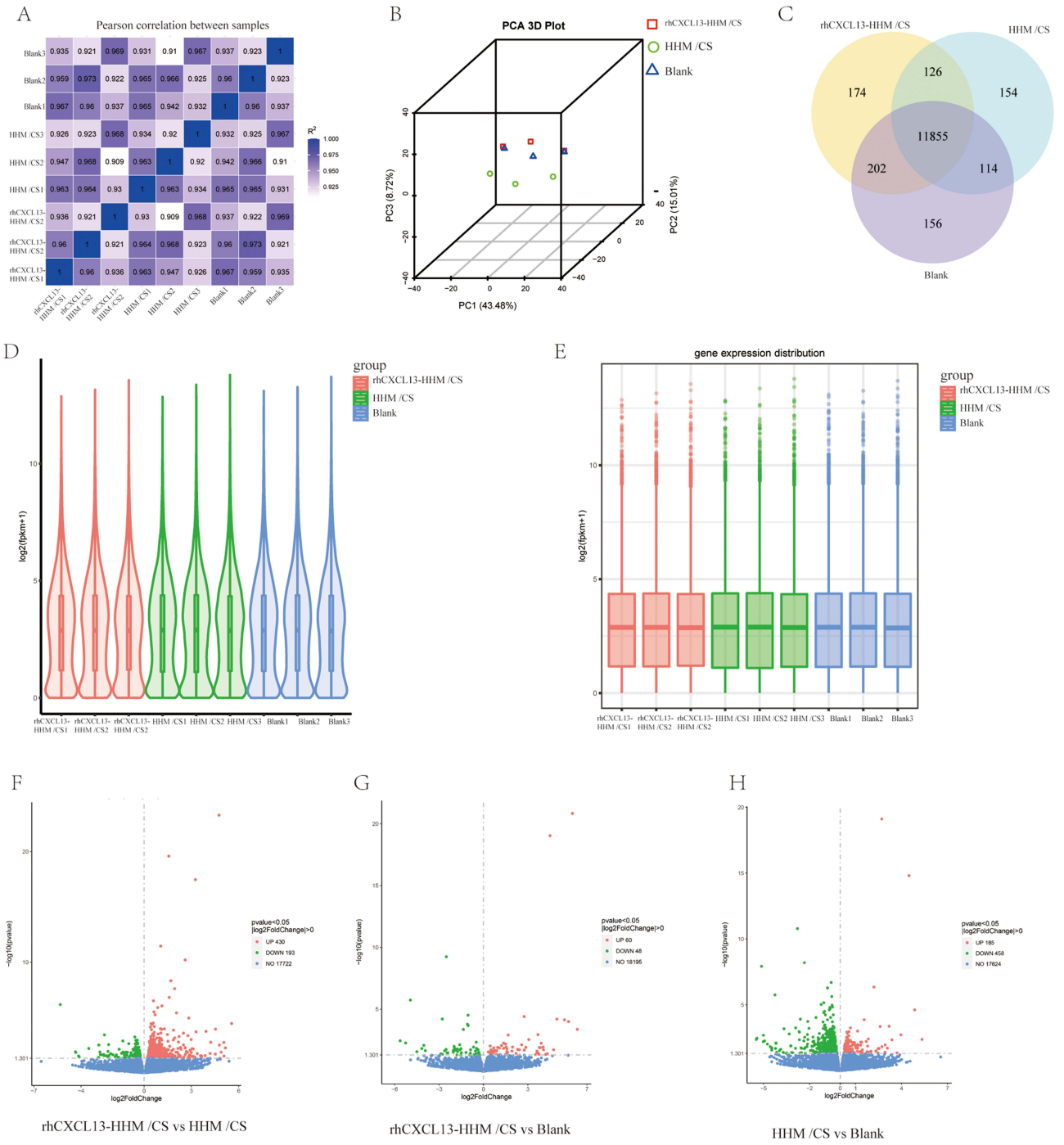

Figure 6 Transcriptomic Analysis of BMSCs Co-cultured with Various Treatment Groups. (**A**) Pearson correlation analysis in between samples. (**B**) 3D image of Principal Component Analysis (PCA) of different samples. (**C**) Venn diagram of differentially expressed genes in different samples. (**D** and **E**) Violin and Box map of differentially expressed genes as determined by transcriptome analysis. (**F-H**) Volcano plots of the expression of various genes in different samples (n=3).

group, differential expression mainly happens in chemotaxis, cell migration, angiogenesis, extracellular matrix tissue, extracellular structural tissue, external packaging structural tissue, and ossification. The differential expression of the rhCXCL13-HHM/CS group's genes mainly focuses on regulating mitochondrial tissue, cytochrome C release from mitochondria, and cardiomyocyte apoptosis. The bubble chart of differentially expressed genes under the GO up enrichment analysis is displayed (Figure 7C1-C3). The distribution of all differentially expressed genes in each group is presented through a heatmap. Although both the HHM/CS group and

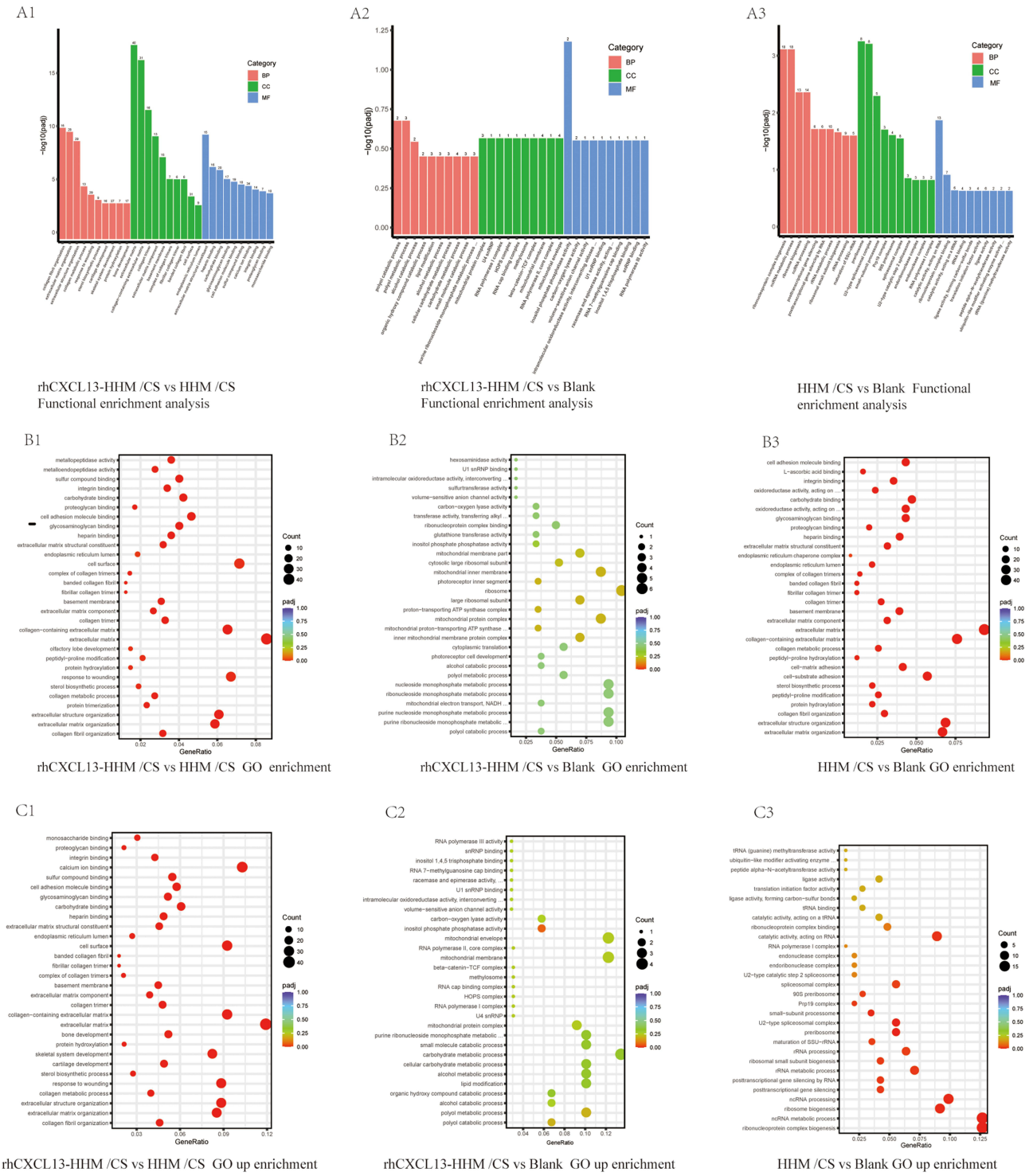

Figure 7 Functional and GO Enrichment Analysis of BMSCs Co-cultured with Various Treatment Groups. (**A1-A3**) Functional enrichment analysis conducted in terms of biological processes, cell components, and molecular functions. (**B1-B3**) Bubble Map of differentially expressed genes based on GO Enrichment Analysis. (**C1-C3**) GO enrichment of the up-regulated expressions of Various Treatment Groups.

rhCXCL13-HHM/CS group can promote bone healing, their inherent mechanisms may not be identical. (Figure 8A). KEGG up pathway enrichment analysis was applied to ascertain the pathway enrichment of differentially expressed genes (Figure 8C1-C3). By contrasting the rhCXCL13-HHM/CS and the HHM/CS groups, it was identified that the primary pathways of the differentially expressed genes were associated with the PI3K −

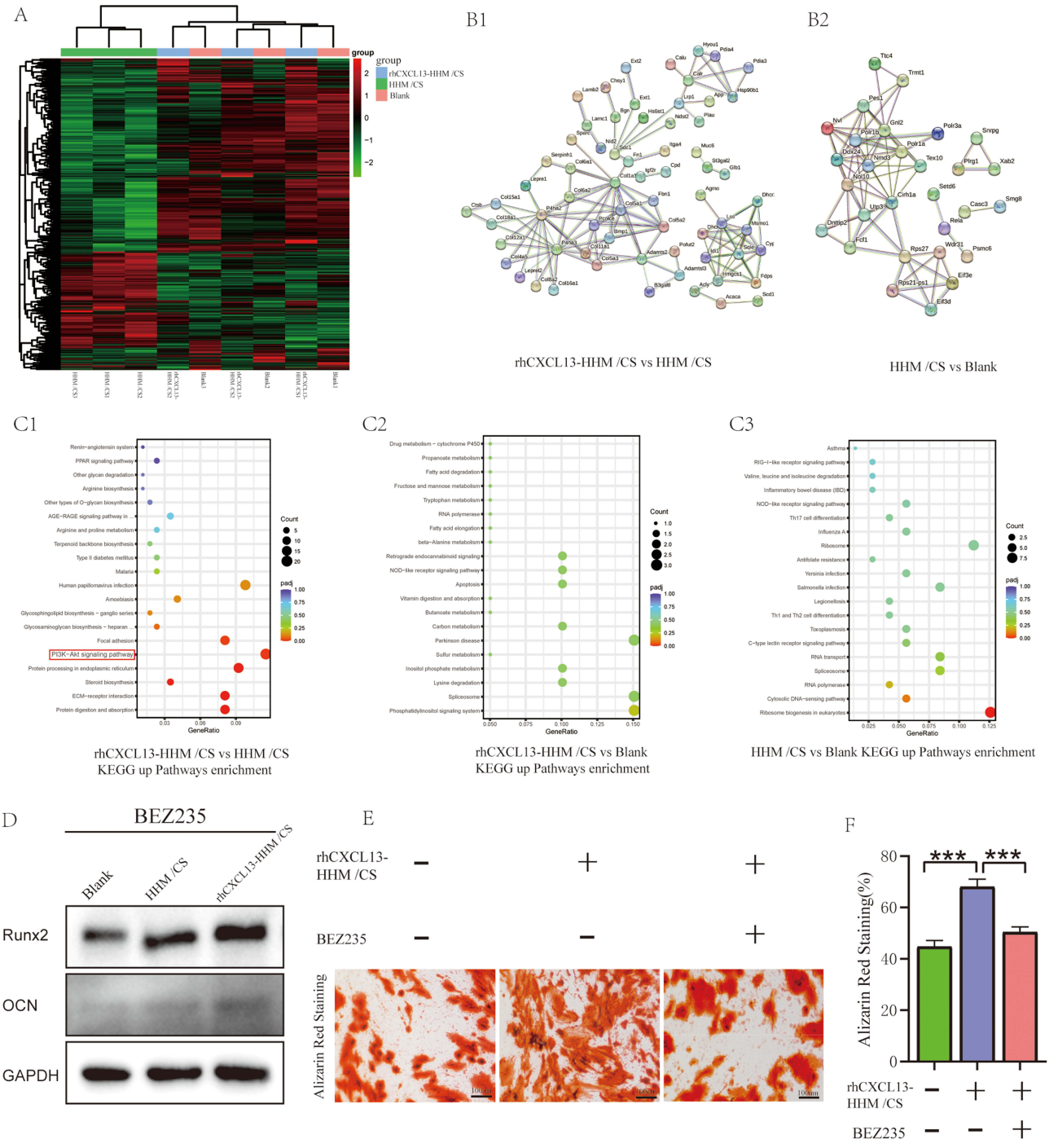

Figure 8 Heat Map, Protein-Protein Interaction (PPI) Network, and KEGG Up-Pathway Enrichment Analyses in Various Treatment Groups. (**A**) Heat Map of differentially expressed genes related to cellular activity, osteogenesis, angiogenesis, and BMSC recruitment in different groups comparisons. (**B1** and **B2**) PPI analysis revealing the function of DEG-encoded proteins in different groups. (**C1-C3**) KEGG up-pathway enrichment analysis in different groups comparisons. The red symbol in (**C1**) indicates that the KEGG up-pathway enrichment analysis of differentially expressed genes mainly concentrated in the PI3K-AKT signaling pathway. (**D**) Changes in the relative gene expression levels of RUNX2 and OCN after treatment with PI3K-AKT inhibitor BEZ235 in BMSCs from all groups. (**E**) Representative alizarin red staining image of BMSCs co-cultured with rhCXCL13-HHM/CS scaffold after 21 days of osteogenic differentiation treated with PI3K-AKT inhibitor BEZ235 (scale bar = 100μm, n=3). (**F**) Quantitative analysis of alizarin red staining of BMSCs in different treatment groups (***p<0.001, n=3).

AKT signaling pathway, protein digestion and absorption, and the human papillomavirus infection pathway (Figure 8C1).

In addition, protein-protein interaction network (PPI) analysis reveals the protein function encoded by DEG in different groups. The enrichment of GO and KEGG confirms that the leading network is related to collagen and extracellular space. A collagen-related network with differential gene expression is found between HHM/CS and Blank groups and between rhCXCL13-HHM/CS and HHM/C groups (Col1a1, Col5a1, Col6a1, Etc.) (Figure 8B1 and B2). Validation of the osteogenic mechanism is conducted based on the results of transcriptome sequencing analysis. When the PI3K-AKT inhibitor BEZ235 was added to each treatment group, the protein expression of RUNX2 and OCN decreased compared to the without BEZ235 groups (Figure 8D). This was further confirmed by Alizarin red staining image of BMSCs co-cultured with rhCXCL13-HHM/CS scaffold after 21 days of osteogenic differentiation with BEZ235 treatment (Figure 8E). A quantitative statistical analysis further demonstrated that the osteogenic differentiation capacity of BMSCs treated with BEZ235 was significantly lower than that of the rhCXCL13-HHM/CS group (Figure 8F). This provides evidence for the rhCXCL13-HHM/CS's osteogenic mechanism through the PI3K-AKT pathway, a conclusion reinforced by the consistency between the transcriptome data analysis and the experimental results.

Animal Experiment

Gross Anatomy Observation

Four weeks after surgery, the Blank group forms hematomas and granulation tissue. Synovial tissue connects the defective bone. The boundary of the bone defect area is clear. In the HHM/CS and rhCXCL13-HHM/CS groups, bone defects are filled with hematomas and fibrous tissue. The material starts to degrade. Spaces between the material and the bone defect are a little vague and soft, which can be easily penetrated with a needle. Eight weeks after surgery, no callus is formed in the bone defect of the Blank. The materials in HHM/CS and rhCXCL13-HHM/CS are partially degraded and covered with bone tissue. The callus formation of rhCXCL13-HHM/CS is higher than the HHM/CS. Twelve weeks after surgery, the Blank has no callus formation or bone nonunion in the bone defect, and the medullary cavity is closed. The materials in HHM/CS and rhCXCL13-HHM/CS are basically degraded, and the bone defect is completely repaired and healed (Figure 9A).

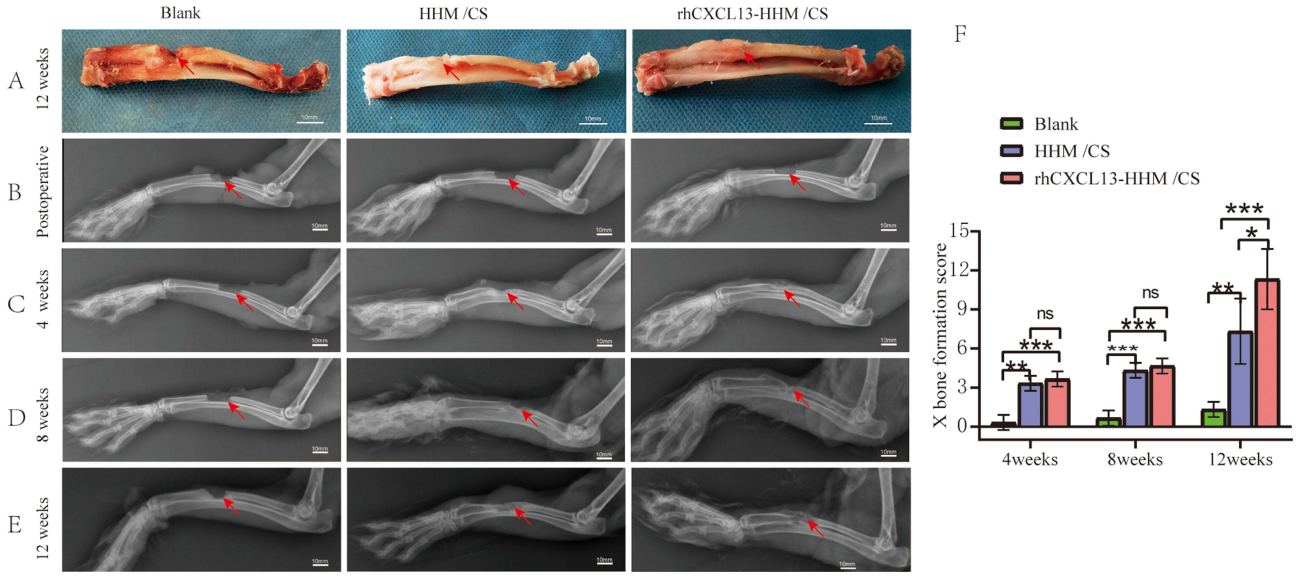

Figure 9 Postoperative gross observation and X-ray analysis: (**A**) Gross observation of bone healing 12 weeks after surgery. (**B**) X-ray imaging immediately after surgery. (**C**) X-ray imaging at 4 weeks postoperative. (**D**) X-ray imaging at 8 weeks postoperative. (**E**) X-ray imaging at 12 weeks postoperative. (**F**) Bone formation scoring analysis, indicating superior bone healing in the rhCXCL13-HHM/CS group compared to the HHM/CS and blank groups. Statistical analysis was performed using ANOVA and LSD tests, with results expressed as mean ± SD (*p < 0.05, **p < 0.01, ***p < 0.001, n=3).
Abbreviation: ns, Not statistical significance.

X-Ray Analysis

All experimental animals were immediately X-ray after making bone defect models (Figure 9B). Four weeks after surgery, the X-ray shows no callus formation at the fracture of the radius defect in the Blank. In the HHM/CS and rhCXCL13-HHM/CS, the materials for bone defect are slightly degraded, and a small amount of callus formation occurs. The boundary between the material and defective bone is blurred (Figure 9C). Eight weeks after surgery, no callus is formed at the bone defect in the Blank, and the fracture end is smooth. The materials in the HHM/CS and rhCXCL13-HHM/CS are further degraded, and calluses larger than in four weeks are formed. The rhCXCL13-HHM/CS has a broader callus formation than the HHM/CS (Figure 9D). After 12 weeks, no callus formation occurs in the Blank, indicating bone nonunion. The materials in the HHM/CS group and rhCXCL13-HHM/CS groups are basically degraded, and a completely bridging callus is formed. The bone defect is repaired with the bone healing structure in the rhCXCL13-HHM/CS better than in the HHM/CS group (Figure 9E). The radius defect healing score at each time point is calculated according to the Lane-sandhu-X Ray bone formation score. The statistical analysis shows that healing in the rhCXCL13-HHM/CS is better than in the HHM/CS and Blank groups (Figure 9F).

Three-Dimensional (3D) Reconstructions through Computer Tomography (CT) Analysis

To evaluate the effectiveness of the radial defect model, three-dimensional reconstruction and sagittal CT images were performed immediately after surgery (Figure 10A1 and A2). Three-dimensional (3D) CT imaging assesses

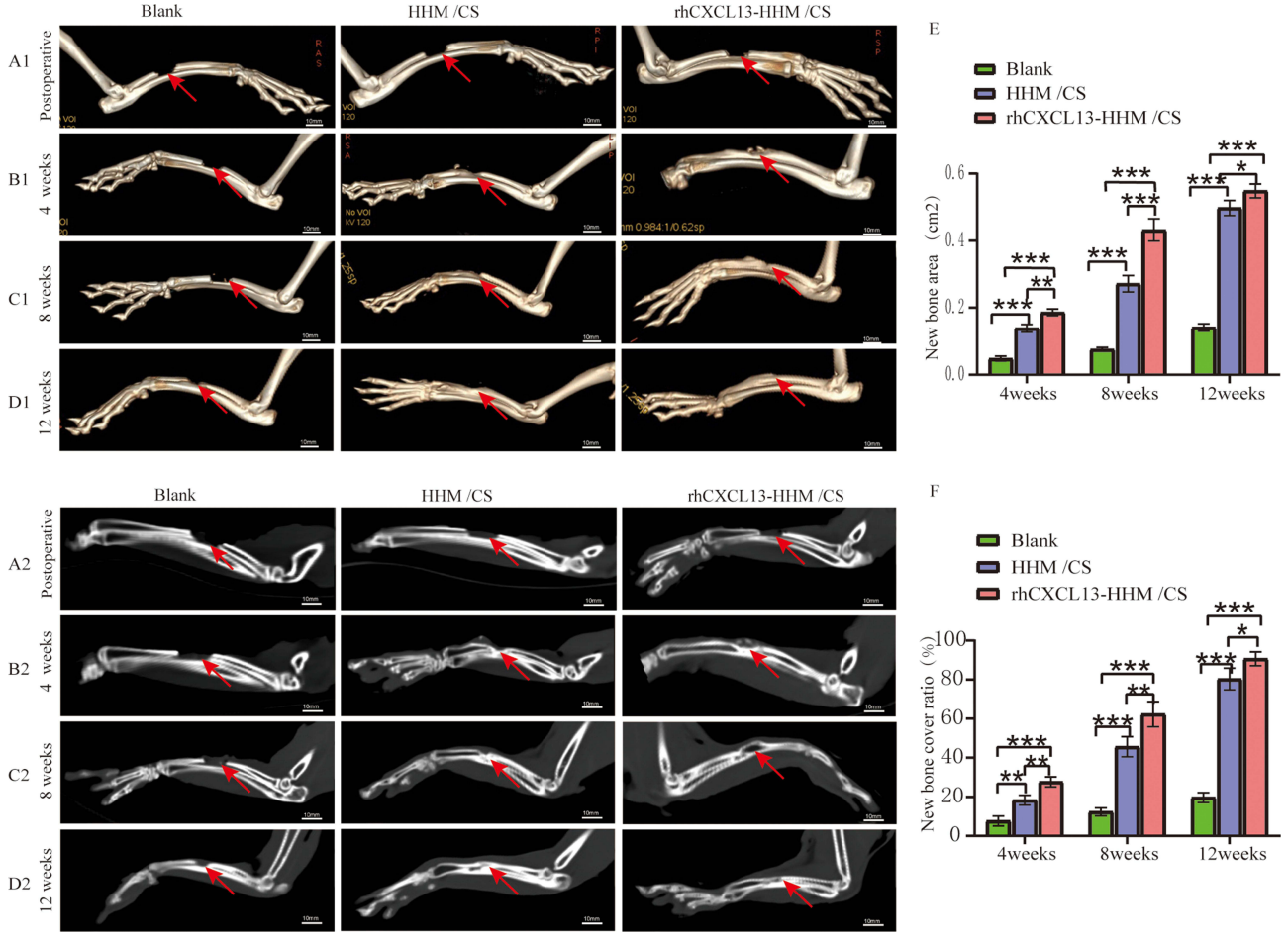

Figure 10 Postoperative CT Analyses of Radial Bone Defects: (**A**) Immediate postoperative 3D and sagittal CT (**A1** and **A2**). (**B**) 4-week postoperative 3D and sagittal CT (**B1** and **B2**). (**C**) 8-week postoperative 3D and sagittal CT (**C1** and **C2**). (**D**) 12-week postoperative 3D and sagittal CT (**D1** and **D2**). (**E**) Statistical analysis of new bone area and coverage across groups using 3D and sagittal CT at 4, 8, and 12 weeks postoperative (**E** and **F**). Data analyzed by ANOVA and LSD tests, expressed as mean ± SD (*p < 0.05, **p < 0.01, ***p < 0.001, n=3).

bone regeneration in bone defects. As shown in the figure of sagittal CT and 3D reconstruction, the bone defects in the Blank groups are barely healed. The bone formation in the defective bones implanted with rhCXCL13-HHM/CS scaffold is better than with the HHM/CS scaffold. Specifically, in week 4, no callus forms in the Blank groups, whereas the HHM/CS and rhCXCL13-HHM/CS scaffold show distinctive callus formation and a small amount of material degradation on the defect margins (Figure 10B1 and B2). No significant difference occurs in callus formation between the HHM/CS and rhCXCL13-HHM/CS groups. However, in week 8, the materials in the rhCXCL13-HHM/CS and HHM/CS scaffolds were further degraded, and the formation of cloud-shaped calluses is visible in the defect. The callus formation of the rhCXCL13-HHM/CS scaffold is significantly better than the other two groups (Figure 10C1 and C2). On the contrary, the Blank group has no new callus, and only a little fibrous connective tissue appears on the defect margins. In week 12, the rhCXCL13-HHM/CS scaffold has a new bone cortex and bone trabecula (Figure 10D1 and D2). The materials are thoroughly degraded, and the bone defects heal. Moreover, most of the materials in the HHM/CS scaffold are degraded, and the bone defects are basically healed. In the Blank groups, the medullary cavities in the defect bones are closed without bone healing. A quantitative analysis of new bone is made (Figure 10E and F). The rhCXCL13-HHM/CS group presents the most significant new bone volume in the 8th and 12th week compared with other groups for the regenerated bone area. In conclusion, rhCXCL13-HHM/CS has good osteogenic capacity.

Histological Analysis

In week 4 (Figure 11A1-A3 and B1-B3), the histological sections stained with H&E show that inflammatory cells and fibrous tissue proliferate in the Blank group. The materials in the HHM/CS and rhCXCL13-HHM/CS are slightly degraded. Fibrous tissue and inflammatory macrophages are intertwined in the defect area with no neovascularization ingrowth. Masson's trichrome staining detects few collagen fiber formations in the Blank group. More Collagen fiber formation is discovered in the HHM/CS group and rhCXCL13-HHM/CS group. In week 8 (Figure 11A4-A6 and B4-B6), a few fibrous tissues are formed and collagenized under the H&E in the Blank groups. Masson's trichrome staining found no cartilage or new bone tissue. The materials in the HHM/CS and rhCXCL13-HHM/CS groups are further degraded and absorbed, and abundant mature collagen, new vessels, and cartilage cells are detected around. The columnar organization of proliferative chondrocytes and new bone is visible. The defect is filled with mineralized bone, and new bones gradually replace the scaffolds. The rhCXCL13-HHM/CS has more bone trabeculae and bone formation than the HHM/CS. In week 12 (Figure 11A7-A9 and B7-B9), no new bone is formed under H&E staining in the Blank group, with only a few inflammatory cells. In HHM/CS, the materials are almost degraded, many new bone tissues are replaced, and the bone defects are basically repaired. The materials of the rhCXCL13-HHM/CS are degraded, and newly formed bone and blood vessels are found. The spaces between mature bone trabeculae are filled with bone marrow. Numerous lamellar bones are formed and completely heal the detective bones. Masson's trichrome staining detects many mature collagen fibers, visualized in blue. The rhCXCL13-HHM/CS obtains new bone formation and mature collagen, which is superior to the HHM/CS and Blank group and indicates a better osteogenic ability.

Immunohistochemistry Analysis

The osteogenesis in the scaffold is further studied by immunohistochemistry. In weeks 4, 8 and 12, Runx2 and BMP-2 immunohistochemical staining are conducted to study osteogenic protein expression in bone regeneration (Figure 12). The positive staining of Runx2 and BMP-2 can be observed in week 4 (Figure 12A1-A3 and B1-B3), which indicates the osteogenic differentiation mediated by the scaffold. In the 8th and 12th week, the positive expression of Runx2 and BMP-2 in the rhCXCL13-HHM/CS is significantly higher than in other groups, representing a stronger osteogenic differentiation ability (Figure 12A4-A9 and B4-B9). These results confirm that rhCXCL13-HHM/CS promotes bone growth and accelerates bone defect healing.

Discussion

The engineered rhCXCL13-HHM/CS bionic scaffold, designed to emulate the composition and structure of bone matrix, promotes both in vitro proliferation and osteogenic differentiation of BMSCs, and fosters the repair of bone defects in vivo. With its high porosity, stable, interconnected porous structure and tissue-adhesive properties, the scaffold fosters

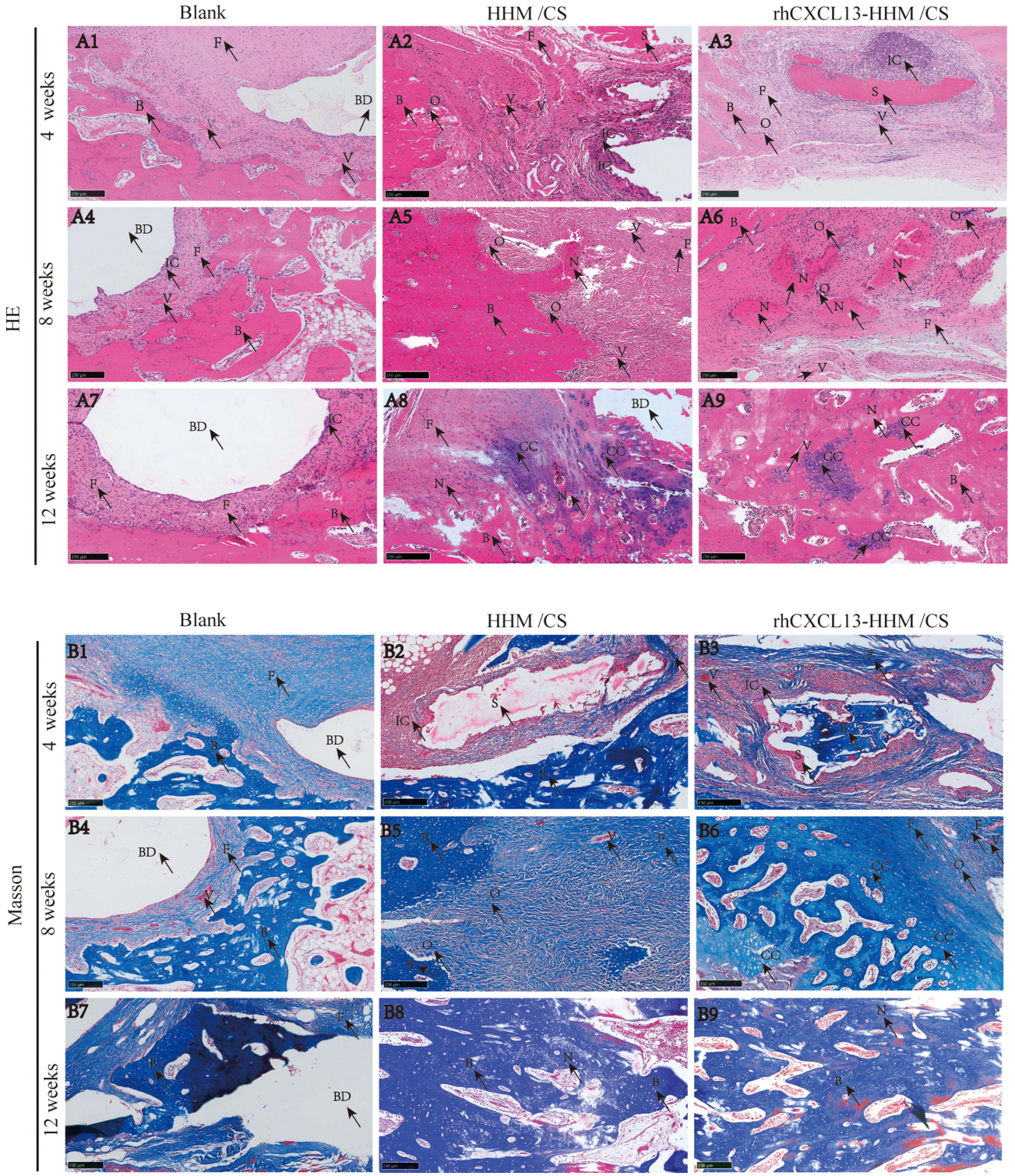

Figure 11 H&E and Masson Staining of Bone Defect Repair Across Different Groups: (**A**) Representative H&E staining images of bone defect repair at 4, 8, and 12 weeks in different groups. (**A1-A9**). (**B**) Representative Masson Staining images of bone defect repair at 4, 8, and 12 weeks in different groups. (**B1-B9**). The H&E and Masson Staining analysis of bone defect repair in rhCXCL13-HHM/CS scaffold is superior to other groups, indicating a better bone repair effect.
Abbreviations: V, new vessel; N, new bone; S, scaffold; O, osteoblast; IC, Inflammatory cell; F, fibrous tissue; CC, cartilage cells; BD, Bone defect.

cell growth, vascularization, and tissue remodeling. Hollow hydroxyapatite microspheres feature unique spherical wall structures, extensive surface areas, hollow interiors, and mesopores (2–8nm) on the surface.This distinct structure enhances drug loading, allowing a broad array of active molecules to achieve sustained and controlled release, thereby

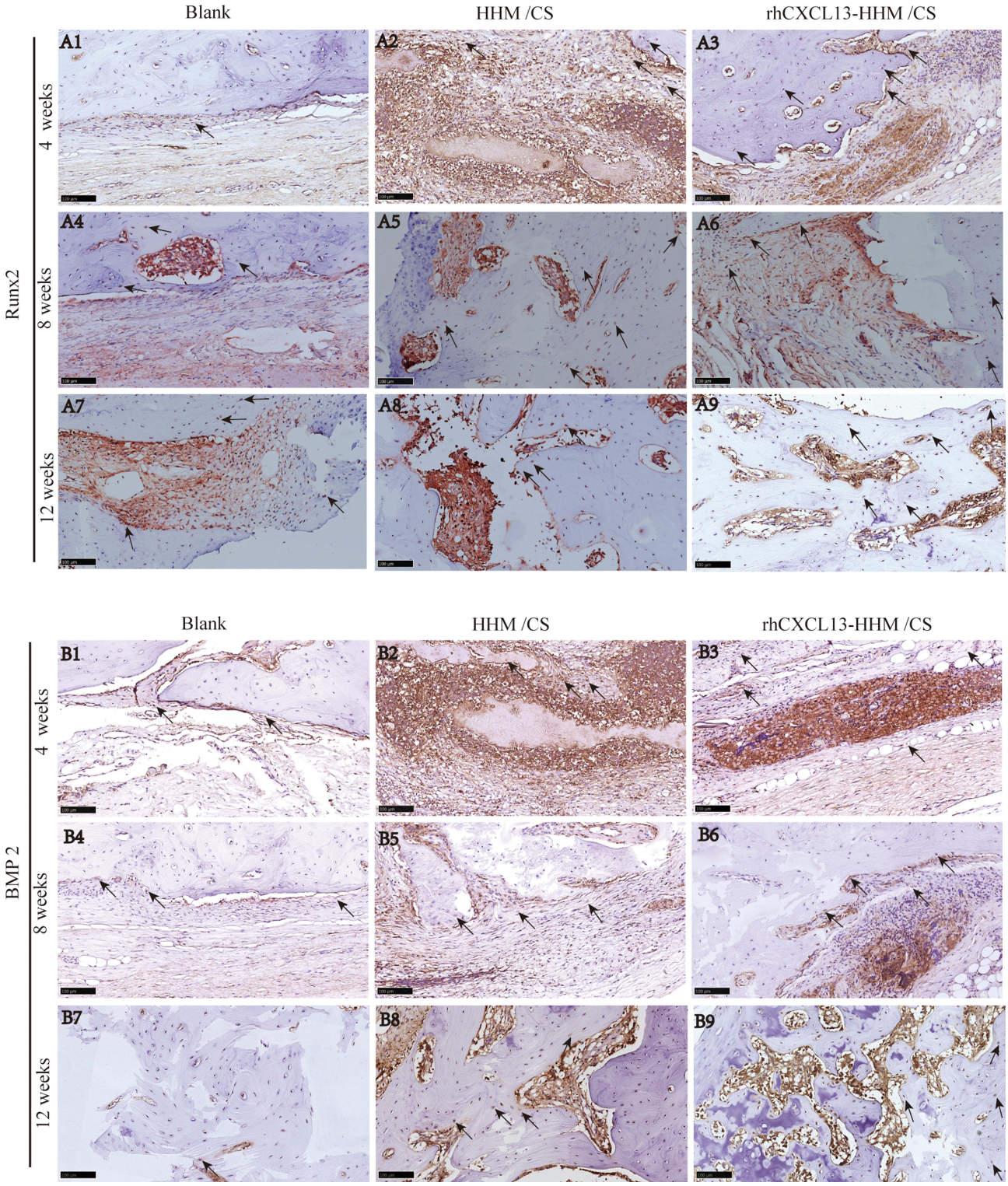

Figure 12 Immunohistochemical Analysis of Bone Defect Repair Across Different Groups: (**A**) Representative immunohistochemical staining images of Runx2 in bone defect repair at 4, 8, and 12 weeks in different groups. (**A1-A9**). (**B**) Representative immunohistochemical staining images of BMP2 in bone defect repair at 4, 8, and 12 weeks in different groups (**B1-B9**). The positive expression of Runx2 and BMP2 in rhCXCL13-HHM/CS scaffold is superior to other groups, indicating its stronger osteogenic differentiation ability (n=3).

improving prolonged release effects. Thus, the hollow hydroxyapatite scaffold serves as an ideal drug carrier. In previous studies,[14] the researchers constructed a hollow hydroxyapatite scaffold loaded with recombinant human bone morphogenetic protein-2, which has a good radius defect repair performance in rabbit experiments. The rhCXCL13 of rhCXCL13-HHM/CS scaffold exhibited a 35-day in vitro release period, demonstrating an initial burst release effect within the first three days. This is attributed to the immediate dissolution and release of rhCXCL13 adsorbed on the microsphere surface upon PBS contact. After this period, rhCXCL13-HHM/CS showcased excellent sustained release capabilities. HHM/CS's porosity significantly increased the storage time of biological factors and had profoundly impacted the drug release rate, which can be attributed to the following reasons. Firstly, the HHM/CS scaffold has a large specific surface area. The rhCXCL13 released from the surface area is easily re-adsorbed by the vacant surface mesopores, reducing the drug release.[20] Secondly, the rhCXCL13 loaded on the scaffold is released at a low concentration through the concentration gradient. Furthermore, the HHM/CS scaffold has a thick shell, resulting in considerable resistance to rhCXCL13 release and reducing the drug release rates. Finally, the surface zeta potential and negative charge density of HHM/CS are high,[13] contributing to a strong adsorption capability for the rhCXCL13.

Biocompatibility is the basis of implantable materials, and implantable biomaterials should have perfect biocompatibility and non-toxicity.[17] In this context, researchers evaluate the in vitro biocompatibility and cell proliferation of rhCXCL13HHM/CS and HHM/CS. The CCK8 assay substantiates that the material can significantly enhance the proliferation of BMSCs on the third and fourth days, primarily due to the scaffold and addition of rhCXCL13 which augments cell proliferation and diffusion. The live/dead staining results confirm that both the HHM/CS and rhCXCL13-HHM/CS scaffolds exhibit superior biocompatibility and non-toxicity. Further, the EDU proliferation assay demonstrates that the rhCXCL13-HHM/CS and HHM/CS scaffolds foster the proliferation of BMSCs, with significant differences being noted between the groups. On a related note, angiogenesis underlies osteogenesis,[21] and as such, implantable biomaterials should have well-established osteogenesis and angiogenesis.[22] Accordingly, the researchers have evaluated the in vitro osteogenesis functions of rhCXCL13-HHM/CS and HHM/CS. The results of cell co-culture prove that the rhCXCL13-HHM/CS scaffold can mimic a matrix microenvironment, thereby significantly enhancing the proliferation and osteoblastic differentiation of BMSCs. Transwell assays clearly indicate that the rhCXCL13-HHM/CS scaffold can accelerate the directional migration of BMSCs towards rhCXCL13 and stimulate the aggregation and proliferation of BMSCs. BMSCs are capable of directional migration towards target tissues, and can endure under the influence of chemokines, inflammatory factors, and other signaling molecules to form stem cell niches. In this local microenvironment, BMSCs can proliferate, differentiate and repair damaged tissues.[23,24]

The homing of MSCs fosters bone repair, encompassing processes such as cell recruitment, migration, proliferation, and differentiation. MSCs play a vital role in modulating the inflammatory response, secreting cytokines, facilitating osteogenic differentiation, and promoting vascular regeneration within a bone defect microenvironment.[25] The process of spontaneous endogenous cell growth into a reconstructed radius is inherently slow, making the repair of substantial bone defects using non-biological factors or cell scaffolds alone a daunting challenge. Previous studies mainly focused on implants combined with exogenous biological factors or cells for skull reconstruction.[26,27] These efforts seek to stimulate bone regeneration by boosting bone differentiation. In this study, we provide in vivo evidence that the scaffold rhCXCL13-HHM/CS can promote cell proliferation and osteoblastic differentiation via the in-situ recruitment of BMSCs. BMSCs are induced to move toward the injury site and reconstruct the osteogenic microenvironment, thus establishing an active "chemotactic core" to facilitate BMSC involvement in osteogenesis. This process is integral to the stem cells' role in enhancing the bone repair process. Consequently, this process promotes rapid angiogenesis and bone repair in defects in the radius of rabbits. This scaffold mimics a natural extracellular matrix, facilitating the attachment, growth, and differentiation of endogenous cells into mature bone tissue, and thus enhancing bone regeneration capabilities. Our study further demonstrates that chemotactic BMSCs possess not only the ability to migrate to injury sites but also robust osteoinductive potential. Bone tissue is known to secrete a plethora of cytokines and chemokines. The latter are classified into four specific subclasses, namely C, CC, CXC, and CX3C, based on the number and spatial arrangement of N-terminal cysteine residues.[28,29] By binding to G protein-coupled receptors on the cell membrane, chemokines stimulate target cells to migrate in a directional manner. By binding to G protein-coupled receptors on the cell membrane, chemokines stimulate target cells to migrate in a directional manner.[9] In MSCs of patients with non-

traumatic osteonecrosis, the expression level of CXCL13 is low, which aligns with diminished osteogenic activity and differentiation potential.[30]

To further analyze the osteogenic differentiation mechanism of rhCXCL13-HHM/CS, transcriptome sequencing is conducted. For the HHM/CS group, distinct expression alterations mainly transpired in domains encompassing chemotaxis, cell migration, angiogenesis, extracellular matrix tissue, extracellular structural tissue, external packaging structural tissue, and ossification. In contrast, the differential expression of the rhCXCL13-HHM/CS group's genes mainly focuses on regulating mitochondrial tissue, cytochrome C release from mitochondria, and cardiomyocyte apoptosis. In the literature, it's been reported that[31] Orthopedic implants targeting mitochondria can restore mitochondrial dynamics and normalize senescent MSCs, thereby enhancing their osteogenic potential. As a result, the local microenvironment of MSCs can be modulated by drug, cell, or bone material transplantation, consequently altering the functionality and tissue orientation of MSCs.[32] When juxtaposed with HHM/CS, the rhCXCL13-HHM/CS scaffold significantly increases chemokine activity and cell recruitment, promoting osteogenesis and angiogenesis, especially through the PI3K-AKT signaling pathway. As such, a conjecture was formed that the extracellular matrix-related proteins of BMSCs could act chemotactically, migrate to injury sites, and possess robust osteogenic capacity.[33] Scaffolds with particular structures can enrich chemokines, and the surface topological structure of the scaffold may induce cell deformation and govern gene expression,[34] such as CXCL13-CXCR5. Transcriptome analysis of rhCXCL13-HHM/CS corroborates that the genes Ecsh1, CXCL12, and Zfp622 are up-regulated, playing an instrumental role in BMSC recruitment.

The KEGG pathway enrichment analysis indicates that differentially expressed genes primarily involve the PI3K-AKT signaling pathway, protein digestion and absorption, and human papillomavirus infection pathway among others. Prior studies have indicated that scaffolds can facilitate BMSC proliferation and enhance angiogenesis and osteogenesis,[35,36] with the PI3K-AKT signaling pathway emerging as the most enriched. Consequently, this pathway may be intertwined with the osteogenic mechanism of rhCXCL13-HHM/CS. The addition of the PI3K-AKT inhibitor BEZ235 reversed the impact of the rhCXCL13-HHM/CS scaffold on RUNX2 and OCN protein expression as well as osteogenic differentiation in BMSCs, thereby demonstrating the rhCXCL13-HHM/CS scaffold's osteogenic mechanism via the PI3K-AKT pathway. Furthermore, the introduction of rhCXCL13 into the HHM/CS scaffold was found to activate the expression of osteogenic-related proteins, enhancing the recruitment of BMSCs. This data suggests that rhCXCL13-HHM/CS promote BMSC recruitment via rhCXCL13, which could improve the functionality of the extracellular matrix and bolster osteogenesis.

How does scaffold morphology exert biological effects? Scaffold morphology significantly influences the biological responses and outcomes following its implantation, A variety of mechanisms have been proposed in the literature[37–39] to explain how scaffold morphology and structure could stimulate osteogenesis and angiogenesis, such as bone immune response,[40] endoplasmic reticulum stress mechanism,[41] and paracrine signaling,[42] among others. When a scaffold is implanted in vivo, the cells adhere to the material surface. The morphology of the scaffold triggers cellular deformation, leading to changes in cell surface pressure and internal tension. This shift initiates a cascade of cellular responses. The transformation of biomechanical signals represents the key mechanism through which scaffold morphology exercises its biological effects. These biomechanical signals are vital in modulating physiological processes, such as maintaining cell behavior and function,[43] which are crucial to bone development and growth. The osteogenesis density of rhCXCL13-HHM/CS scaffolds increased after one month of implantation. This angiogenesis likely results from the high porosity of the scaffold and the influence of the recruited BMSCs on the regulation of osteogenesis and angiogenesis through Runx2 and VEGF expression.[44] Concurrently, the scaffolds provide stable mechanical support within a certain period, ensure structural integrity, and facilitating the development and maturation of blood vessels. Three months post-implantation, the radius defect was successfully repaired by the rhCXCL13-HHM/CS scaffold, demonstrating effective chemotaxis, migration, and osteogenesis abilities of BMSCs. This effectiveness manifested as rapid and extensive endogenous bone regeneration. CT and X-ray confirmed that the bone coverage area was around 95%. Histological analysis and immunofluorescence staining confirm that the bone defect reconstruction sites of both groups contained abundant mineralized bone matrix, with rhCXCL13-HHM/CS outperforming HHM/CS. WB and RT-qPCR results

indicated an increased expression of osteogenesis-related genes and proteins, with rhCXCL13-HHM/CS showing a higher expression level compared to HHM/CS. Due to the positive feedback mechanism, the high expression of Runx2 can further enhance VEGF secretion and stimulate angiogenesis.[45] In conclusion, the rhCXCL13-HHM/CS scaffold emulates the extracellular matrix and recruits bone marrow mesenchymal stem cells, thereby enhancing the ability of endogenous cells to attach, proliferate and differentiate into mature bone tissue. Our study demonstrates the critical influence of scaffold morphology and the distinctive role of the rhCXCL13-HHM/CS scaffold in accelerating bone repair by facilitating targeted cell recruitment and fostering endogenous bone formation.

Conclusion

This study successfully fabricated a biomimetic rhCXCL13-HHM/CS scaffold, mimicking natural bone structure. Its distinct characteristics, such as porous surface, hollow structure, high specific surface area, and nano-channels, position it as a promising tool in drug delivery, bone induction, and controlled drug release. Through a series of in vitro and in vivo studies, the rhCXCL13-HHM/CS scaffold has shown a significantly improved capacity for bone marrow stromal cell (BMSC) recruitment, osteogenesis, and angiogenesis compared to the standard HHM/CS scaffolds. These findings suggest the excellent potential of the rhCXCL13-HHM/CS scaffold in BMSC recruitment, osteogenesis, vascularized tissue-engineered bone reconstruction, and drug delivery, establishing a solid groundwork for the clinical treatment of extensive bone defects. This offers significant theoretical implications and market application prospects. Despite the promising results of this study, there are some limitations and areas requiring further research: The research primarily focuses on relatively short-term outcomes up to 12 weeks post-surgery. Future studies should consider longer time frames to assess the durability and degradation rate of the scaffold, as well as the sustainability of the enhancements in bone formation and angiogenesis. Furthermore, the processes by which the scaffold recruits BMSCs and promotes bone formation are complex, encompassing a variety of cellular and molecular mechanisms. Deeper exploration into these mechanisms and other possibly involved signaling pathways is therefore warranted.

Data Sharing Statement

The datasets used and/or analyzed during the current study are available from the corresponding author on reasonable request.

Ethics Approval and Consent to Participate

All animal experimental procedures and their care were approved by the Animal Ethics Committee of the Shanghai East Hospital of Tongji University and carried out in accordance with the UK Animals (Scientific Procedures) Act (1986).

Author Contributions

All authors made a significant contribution to the work reported, whether that is in the conception, study design, execution, acquisition of data, analysis, and interpretation, or all these areas; took part in drafting, revising or critically reviewing the article; gave final approval of the version to be published; have agreed on the journal to which the article has been submitted; and agree to be accountable for all aspects of the work. Jianhua Zeng and Shilang Xiong are considered co-first authors.

Funding

This study was financially supported by the National Natural Science Foundation of China (No.82160354, 32060222), Science and Technology Plan Project of Jiangxi Province Health Commission (202120005).

Disclosure

The authors declare that they have no competing interests.

References

1. Sanz-Sánchez I, Sanz-Martín I, Ortiz-Vigón A, et al. Complications in bone-grafting procedures: classification and management. *Periodontol*. 2022;88(1):86–102. doi:10.1111/prd.12413
2. Holmes D. Non-union bone fracture: a quicker fix. *Nature*. 2017;550(7677):S193. doi:10.1038/550S193a
3. Wildemann B, Ignatius A, Leung F, et al. Non-union bone fractures. *Nat Rev Dis Primers*. 2021;7(1):57. doi:10.1038/s41572-021-00289-8
4. Feng Z, Jin M, Liang J, et al. Insight into the effect of biomaterials on osteogenic differentiation of mesenchymal stem cells: a review from a mitochondrial perspective. *Acta Biomater*. 2023. doi:10.1016/j.actbio.2023.03.032
5. Chen S, Chen X, Geng Z, et al. The horizon of bone organoid: a perspective on construction and application. *Bioact Mater*. 2022;18:15–25. doi:10.1016/j.bioactmat.2022.01.048
6. Blanchet X, Langer M, Weber C, et al. Touch of chemokines. *Front Immunol*. 2012;3:175. doi:10.3389/fimmu.2012.00175
7. Zhang X, Huang W, Chen X, et al. CXCR5-overexpressing mesenchymal stromal cells exhibit enhanced homing and can decrease contact hypersensitivity. *Mol Ther*. 2017;25(6):1434–1447. doi:10.1016/j.ymthe.2017.04.004
8. Lin F, Zhu Y, Hu G. Naringin promotes cellular chemokine synthesis and potentiates mesenchymal stromal cell migration via the Ras signaling pathway. *Exp Ther Med*. 2018;16(4):3504–3510. doi:10.3892/etm.2018.6634
9. Tian F, Ji XL, Xiao WA, et al. CXCL13 Promotes Osteogenic Differentiation of Mesenchymal Stem Cells by Inhibiting miR-23a Expression. *Stem Cells Int*. 2015;2015:632305. doi:10.1155/2015/632305
10. Lisignoli G, Toneguzzi S, Piacentini A, et al. CXCL12 (SDF-1) and CXCL13 (BCA-1) chemokines significantly induce proliferation and collagen type I expression in osteoblasts from osteoarthritis patients. *J Cell Physiol*. 2006;206(1):78–85. doi:10.1002/jcp.20435
11. Von Lüttichau I, Notohamiprodjo M, Wechselberger A, et al. Human adult CD34- progenitor cells functionally express the chemokine receptors CCR1, CCR4, CCR7, CXCR5, and CCR10 but not CXCR4. *Stem Cells Dev*. 2005;14(3):329–336. doi:10.1089/scd.2005.14.329
12. Xu M, Liu T, Qin M, et al. Bone-like hydroxyapatite anchored on alginate microspheres for bone regeneration. *Carbohydr Polym*. 2022;287:119330. doi:10.1016/j.carbpol.2022.119330
13. Kai-Ping Z, Jing S, Song Y, et al. A Novel Hollow Hydroxyapatite Microspheres/Chitosan Composite Drug Carrier for Controlled Release. *J Inorganic Materials*. 2016;31(4):434. doi:10.15541/jim20150488
14. Xiong L, Zeng J, Yao A, et al. BMP2-loaded hollow hydroxyapatite microspheres exhibit enhanced osteoinduction and osteogenicity in large bone defects. *Int J Nanomedicine*. 2015;10:517–526. doi:10.2147/ijn.S74677
15. Li J, Xiong S, Ding L, et al. The mechanism research of non-Smad dependent TAK1 signaling pathway in the treatment of bone defects by recombination BMP-2-loaded hollow hydroxyapatite microspheres/chitosan composite. *J Mater Sci Mater Med*. 2019;30(12):130. doi:10.1007/s10856-019-6340-9
16. Hayashi K, Yanagisawa T, Kishida R, et al. Effects of scaffold shape on bone regeneration: tiny shape differences affect the entire system. *ACS Nano*. 2022. doi:10.1021/acsnano.2c03776
17. Sivakumar PM, Yetisgin AA, Sahin SB, et al. Bone tissue engineering: anionic polysaccharides as promising scaffolds. *Carbohydr Polym*. 2022;283:119142. doi:10.1016/j.carbpol.2022.119142
18. Hu X, Zhang P, Xu Z, et al. GPNMB enhances bone regeneration by promoting angiogenesis and osteogenesis: potential role for tissue engineering bone. *J Cell Biochem*. 2013;114(12):2729–2737. doi:10.1002/jcb.24621
19. Filippi M, Dasen B, Guerrero J, et al. Magnetic nanocomposite hydrogels and static magnetic field stimulate the osteoblastic and vasculogenic profile of adipose-derived cells. *Biomaterials*. 2019;223:119468. doi:10.1016/j.biomaterials.2019.119468
20. Xiao W, Fu H, Rahaman MN, et al. Hollow hydroxyapatite microspheres: a novel bioactive and osteoconductive carrier for controlled release of bone morphogenetic protein-2 in bone regeneration. *Acta Biomater*. 2013;9(9):8374–8383. doi:10.1016/j.actbio.2013.05.029
21. Kusumbe AP, Ramasamy SK, Adams RH. Coupling of angiogenesis and osteogenesis by a specific vessel subtype in bone. *Nature*. 2014;507(7492):323–328. doi:10.1038/nature13145
22. Yu Y, Dai K, Gao Z, et al. Sulfated polysaccharide directs therapeutic angiogenesis via endogenous VEGF secretion of macrophages. *Sci Adv*. 2021;7(7). doi:10.1126/sciadv.abd8217
23. Bez M, Sheyn D, Tawackoli W, et al. In situ bone tissue engineering via ultrasound-mediated gene delivery to endogenous progenitor cells in mini-pigs. *Sci Transl Med*. 2017;9(390). doi:10.1126/scitranslmed.aal3128
24. Wells JM, Watt FM. Diverse mechanisms for endogenous regeneration and repair in mammalian organs. *Nature*. 2018;557(7705):322–328. doi:10.1038/s41586-018-0073-7
25. Frenette PS, Pinho S, Lucas D, et al. Mesenchymal stem cell: keystone of the hematopoietic stem cell niche and a stepping-stone for regenerative medicine. *Annu Rev Immunol*. 2013;31:285–316. doi:10.1146/annurev-immunol-032712-095919
26. Zhang X, Li Y, Chen YE, et al. Cell-free 3D scaffold with two-stage delivery of miRNA-26a to regenerate critical-sized bone defects. *Nat Commun*. 2016;7:10376. doi:10.1038/ncomms10376
27. Mochizuki M, Güç E, Park AJ, et al. Growth factors with enhanced syndecan binding generate tonic signalling and promote tissue healing. *Nat Biomed Eng*. 2020;4(4):463–475. doi:10.1038/s41551-019-0469-1
28. Rajagopalan L, Rajarathnam K. Structural basis of chemokine receptor function--a model for binding affinity and ligand selectivity. *Biosci Rep*. 2006;26(5):325–339. doi:10.1007/s10540-006-9025-9
29. Jin T, Xu X, Hereld D. Chemotaxis, chemokine receptors and human disease. *Cytokine*. 2008;44(1):1–8. doi:10.1016/j.cyto.2008.06.017
30. Xu W, Li J, Tian H, et al. MicroRNA-186-5p mediates osteoblastic differentiation and cell viability by targeting CXCL13 in non-traumatic osteonecrosis. *Mol Med Rep*. 2019;20(5):4594–4602. doi:10.3892/mmr.2019.10710
31. Chen M, Wang D, Li M, et al. Nanocatalytic Biofunctional MOF Coating on Titanium Implants Promotes Osteoporotic Bone Regeneration through Cooperative Pro-osteoblastogenesis MSC Reprogramming. *ACS Nano*. 2022;16(9):15397–15412. doi:10.1021/acsnano.2c07200
32. Scadden DT. The stem-cell niche as an entity of action. *Nature*. 2006;441(7097):1075–1079. doi:10.1038/nature04957
33. de Melo Pereira D, Habibovic P. Biomineralization-inspired material design for bone regeneration. *Adv Healthc Mater*. 2018;7(22):e1800700. doi:10.1002/adhm.201800700
34. Liu R, Ding J. Chromosomal repositioning and gene regulation of cells on a micropillar array. *ACS Appl Mater Interfaces*. 2020;12(32):35799–35812. doi:10.1021/acsami.0c05883

35. Lu G, Xu Y, Liu Q, et al. An instantly fixable and self-adaptive scaffold for skull regeneration by autologous stem cell recruitment and angiogenesis. *Nat Commun*. 2022;13(1). doi:10.1038/s41467-022-30243-5
36. Shen WC, Lai YC, Li LH, et al. Methylation and PTEN activation in dental pulp mesenchymal stem cells promotes osteogenesis and reduces oncogenesis. *Nat Commun*. 2019;10(1):2226. doi:10.1038/s41467-019-10197-x
37. Fang H, Zhu D, Yang Q, et al. Emerging zero-dimensional to four-dimensional biomaterials for bone regeneration. *J Nanobiotechnology*. 2022;20 (1):26. doi:10.1186/s12951-021-01228-1
38. Hayashi K, Kato N, Kato M, et al. Impacts of channel direction on bone tissue engineering in 3D-printed carbonate apatite scaffolds. *Mater Des*. 2021:204. doi:10.1016/j.matdes.2021.109686
39. Hayashi K, Tsuchiya A, Shimabukuro M, et al. Multiscale porous scaffolds constructed of carbonate apatite honeycomb granules for bone regeneration. *Mater Des*. 2022;215. doi:10.1016/j.matdes.2022.110468
40. Qiao W, Xie H, Fang J, et al. Sequential activation of heterogeneous macrophage phenotypes is essential for biomaterials-induced bone regeneration. *Biomaterials*. 2021;276:121038. doi:10.1016/j.biomaterials.2021.121038
41. Shi M, Song W, Han T, et al. Role of the unfolded protein response in topography-induced osteogenic differentiation in rat bone marrow mesenchymal stem cells. *Acta Biomater*. 2017;54:175–185. doi:10.1016/j.actbio.2017.03.018
42. Lian M, Sun B, Han Y, et al. A low-temperature-printed hierarchical porous sponge-like scaffold that promotes cell-material interaction and modulates paracrine activity of MSCs for vascularized bone regeneration. *Biomaterials*. 2021;274:120841. doi:10.1016/j.biomaterials.2021.120841
43. Hannezo E, Heisenberg CP. Mechanochemical Feedback Loops in Development and Disease. *Cell*. 2019;178(1):12–25. doi:10.1016/j.cell.2019.05.052
44. Liu Y, Luo D, Yu M, et al. Thermodynamically controlled self-assembly of hierarchically staggered architecture as an osteoinductive alternative to bone autografts. *Adv Funct Mater*. 2019;29(10). doi:10.1002/adfm.201806445
45. Wang C, Lin K, Chang J, et al. Osteogenesis and angiogenesis induced by porous β-CaSiO(3)/PDLGA composite scaffold via activation of AMPK/ERK1/2 and PI3K/Akt pathways. *Biomaterials*. 2013;34(1):64–77. doi:10.1016/j.biomaterials.2012.09.021